University of Tartu

Faculty of Science and Technology

Institute of Physics

Kristjan Eimre

Implementing the general thermal-field emission equation to the high electric field nanoprotrusion model

Bachelor's thesis

Supervisors: PhD Vahur Zadin,
PhD Flyura Djurabekova

Tartu 2015

Contents

Abbreviations and symbols

Abbrevations

CLIC	Compact Linear Collider
RF	radio frequency
FN	Fowler-Nordheim
GTF	general thermal-field
WKB	Wentzel–Kramers–Brillouin
RLD	Richardson Laue Dushman
FEM	finite element method
FDM	finite difference method
ED-MD	electrodynamics - molecular dynamics
HELMOD	hybrid electrodynamics-molecular dynamics

Symbols

Latin letters

F	local electric field (on the metal surface)
F_e	product of the local electric field and elementary charge
E	applied electric field (macroscopic)
T	temperature
J	current density
q	elementary charge
m	mass of electron
h	height of the protrusion
r	radius of the protrusion
d	diameter of the protrusion

Greek letters

Φ	work function of the metal (copper in most cases)
β	field enhancement
β_c	average or effective field enhancement
$\varphi(\boldsymbol{r})$	Electric potential
$\rho(\boldsymbol{r})$	Space charge density
ϵ_0	vacuum permittivity
$\rho(T)$	resistivity of copper
$\sigma(T)$	electrical conductivity
$\kappa(T)$	thermal conductivity

1. Introduction

1.1 Overview of the problem

High electric fields are used in many devices today, such as free electron lasers, fusion reactors and particles accelerators. Even in ultra-high vacuum conditions [1], when the electric field reaches a high enough value, electric discharges (vacuum arcing) occur, which damage the devices [2] or lower their performance. One such application is the planned particle accelerator Compact LInear Collider (CLIC) at CERN [3, 4], which is designed to accelerate electrons and positrons using high radio frequency (RF) electric fields. The performance of the accelerating RF field is limited by a critical value, where the frequency of vacuum discharge events becomes intolerable because of surface damage and the loss of particle bunches. Figure 1.1 shows the copper accelerating structures, where the discharges occur. The CLIC project aims to achieve a RF accelerating field of 100 MV/m at 12 GHz (the corresponding surface field is ~200 MV/m during 200 ns pulses every 20 ms) with a breakdown rate (discharges per RF pulse per meter) under 10^{-6} [5]. Understanding the origins of the electrical breakdowns is important for controlling them at the desired level.

A vacuum discharge goes through three phases: breakdown, a spark and an arc [6]. Breakdown involves phenomena, which create a conductive channel in the vacuum. A spark is a self-sustaining process responsible for the current rise in the vacuum. An arc is the phase, which features a steady current and is terminated when the cathode crater becomes big enough

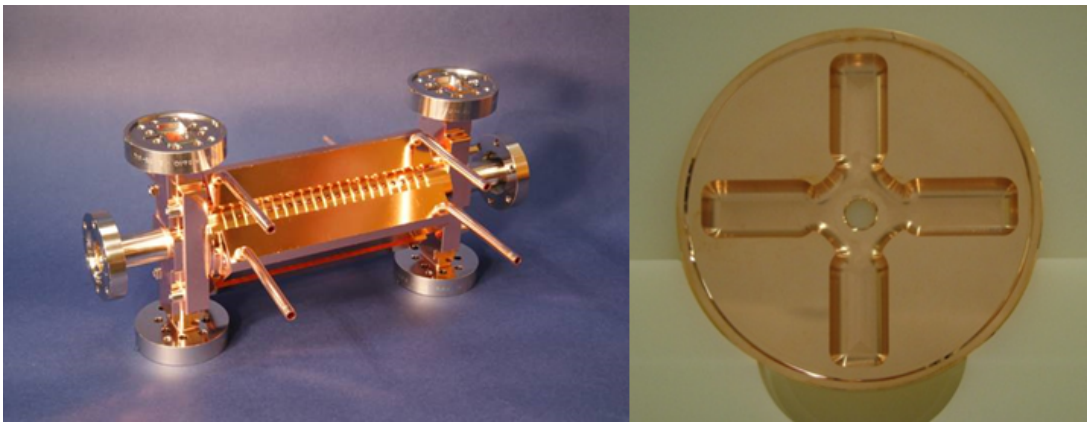

Figure 1.1: CLIC accelerating structure components. Figure taken from [4].

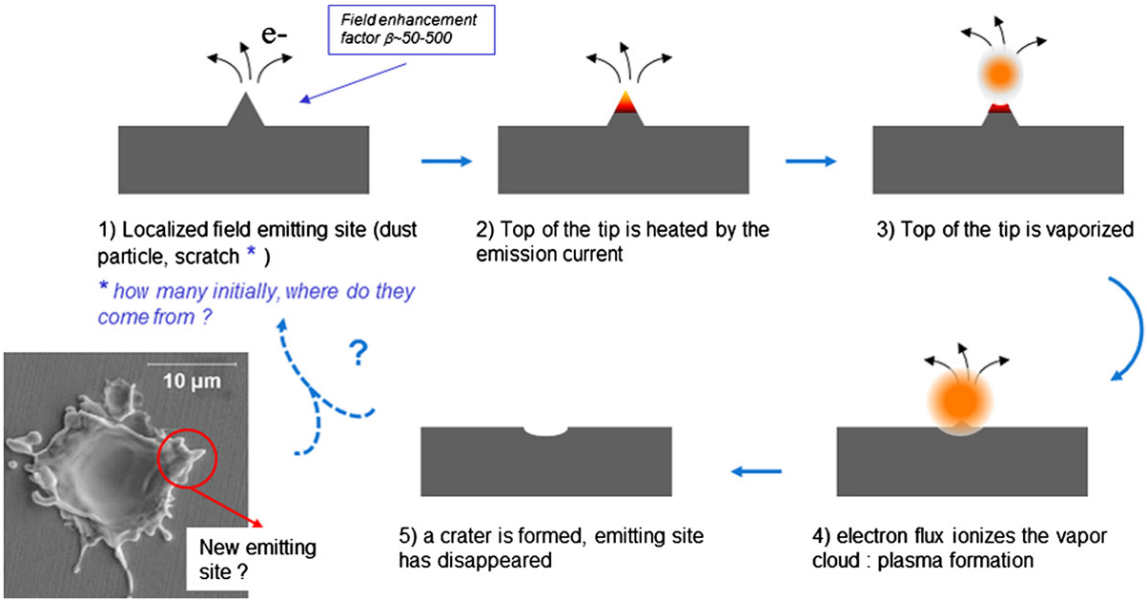

Figure 1.2: The vacuum discharge mechanism. Figure taken from [8].

to not be able to sustain the process any more [7]. The work of the current thesis studies the breakdown mechanisms.

The vacuum breakdown [6, 8] is believed to occur due to multiple [9] nanoscale [10] protrusions on the cathode, where the electric field is locally enhanced by a factor of 10 to 100 [11]. Due to high local electric field, electrons will tunnel through the surface barrier, resulting in emission currents. The currents will heat the protrusions through Joule heating, eventually melting and evaporating the metal. The vapor cloud is ionized through gas multiplication and a conductive medium in the vacuum has been formed. Next, the arc is formed, which leaves a crater behind, where the edges are candidates for new initial protrusions. The process can be seen on figure 1.2. There are also other proposed possibilities for the arcing mechanism (e.g. based on electromigration [8]), but electron emission currents and the resulting Joule heating is a key component in all of them.

The emission currents have traditionally [12–14] been estimated using the Fowler-Nordheim (FN) equation [15], which only considers the quantum tunnelling of electrons from the metal and neglects all thermal effects. However, when dealing with melting protrusions, electrons will also surpass the metal surface barrier (work function) by thermal excitation and thus the FN model is inaccurate.

An emission current model, called the general thermal-field (GTF) equation [16–18] takes also the thermal contribution into account, in addition to the quantum tunnelling effect. At low temperatures and high fields, the GTF equation becomes the FN equation (field emission region) while at higher temperatures and lower fields, it becomes the Richardson-Laue-Dushman (RLD) [19] equation (thermionic emission region). Additionally, the currents in the intermediate region are also accurately represented.

1.2 The objectives of this work

The current thesis summarizes and extends the work published in research article "Application of the general thermal field (GTF) model to simulate the behaviour of nanoscale Cu field emitters" by K. Eimre et. al., submitted to Journal of Applied Physics (included in appendix C).

The general objective was to investigate the electric currents and thermal behaviour of copper nanoprotrusions in similar conditions as in CLIC DC experiments [20, 21] using the GTF emission model. It can be divided into smaller sub-objectives:

- Create a straightforward implementation of the GTF emission equation on the basis of K. L. Jensen et al. theoretical concepts. Implement it into the the finite element method (FEM) nanoprotrusion model. Additionally, create a clear documentation so it could be easily implemented into other systems.
- Find and analyse the electric currents and thermal behaviour of the FEM nanoprotrusion model.
- Compare the behaviour of the system using the GTF emission model to the Fowler-Nordheim model.
- Investigate the thermal effects on the Fowler-Nordheim plot (frequently used to estimate a surface's field enhancement, see section 3.7) introduced by the GTF equation.
- Compare the behaviour of the FEM model with hybrid electrodynamics - molecular dynamics (ED-MD) model (HELMOD, section 3.10).

1.3 Author's contribution

The initial FEM nanoprotrusion model was provided by Vahur Zadin, which the author improved and into which the GTF equation was implemented. The HELMOD results in the research article and this thesis (section 4.5) were provided by Stefan Parviainen from the University of Helsinki.

In the research article, the author obtained all the FEM simulation results. Additionally, all the figures were created by the author and the author wrote the section about emission currents and parts of the analysis.

In the current thesis, all research, writing and figures were done by the author except for figures 1.1 and 1.2.

2. Theoretical overview

2.1 Electron emission

Electron emission current density J from a metal body into vacuum can be expressed as a general integral [16, 22–24]

$$J(F,T) = q \int_{-\infty}^{\infty} N(U,T) D(U,F) dU, \tag{2.1}$$

where F is the electric field at the metal surface, T is the temperature and U is the total energy in the direction normal to the surface of an electron. $N(U,T)$ is the supply function or the number of Fermi-Dirac electrons within the energy range dU incident on the barrier per unit time and surface area. And finally, $D(U,F)$ is the probability that an electron with energy U penetrates the surface potential barrier. Assuming the Fermi-Dirac distribution, the supply function can be expressed as

$$N(U,T) = \frac{4\pi m k_B T}{h_P^3} \ln\left(1 + \exp\left(-\frac{U+\Phi}{k_B T}\right)\right), \tag{2.2}$$

where m is the electron mass, k_B is the Boltzmann constant, h_P is the Planck's constant and Φ is the work function of the metal. And the emission probability can be expressed by using the Wentzel–Kramers–Brillouin (WKB) approximation as

$$D(U,F) = \begin{cases} \left(1 + \exp\left(-\frac{2\sqrt{2m}}{\hbar} \int_{x_-}^{x_+} \sqrt{V(x) - U}\, dx\right)\right)^{-1}, & \text{if } U < V_{\max}, \\ 1, & \text{if } U \geq V_{\max}, \end{cases} \tag{2.3}$$

where $\hbar = h_P/(2\pi)$ and x_-, x_+ are the zeroes of the integrand. The part where $U < V_{\max}$ corresponds to quantum tunnelling and $U \geq V_{\max}$ corresponds to the electron classically surpassing the barrier. $V(x)$ is the surface potential barrier, for which, the Schottky-Nordheim expression [25] is usually used

$$V_{SN}(F,x) = \Phi - qFx - \frac{q^2}{16\pi\epsilon_0 x}, \tag{2.4}$$

where the energies are given relative to the Fermi level (i.e. the Fermi energy U_F is taken to be zero). Φ is the work function, $-qFx$ the effect of the field on the potential barrier and $-\frac{q^2}{16\pi\epsilon_0 x}$ is the image potential factor (emitted electrons are attracted back to the metal due to interactions

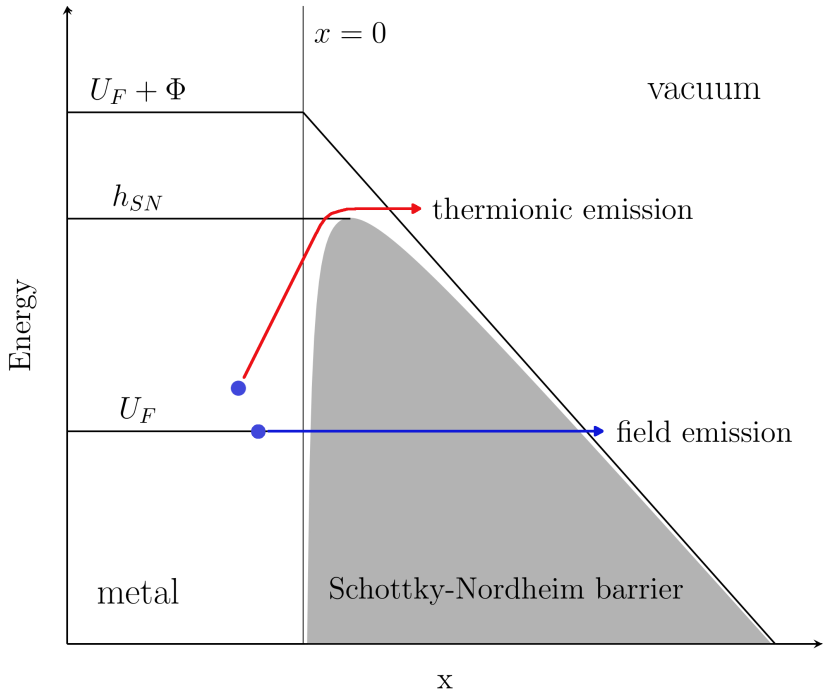

Figure 2.1: Schottky-Nordheim barrier and the principle behind thermionic and field emissions. $x = 0$ is the boundary between metal and vacuum, U_F is the Fermi level and h_{SN} is the maximum height of the barrier.

with the conductive surface). q is the elementary charge and ϵ_0 is the electric constant. Note that x is a coordinate, which is 0 at the metal surface and positive towards vacuum. The barrier can be seen of figure 2.1.

Even though the assumptions made (mainly the WKB approximation in eq. 2.3) are approximative in several ways [24], the treatment up to this point is considered "exact" [22]. The resulting integral of eq. 2.1 can be evaluated numerically [22, 23] but this is computationally intensive and in many applications infeasible and thus analytical expressions are sought by introducing additional approximations.

2.2 Thermionic emission

By assuming that quantum tunnelling does not occur (i.e. in eq. 2.3, the part for $U < V_{\max}$ is equal to zero) then the only way electrons are emitted is by thermal excitation over the surface barrier (see fig. 2.1). This phenomenon is called the thermionic emission and it can be described by the Richardson-Laue-Dushman equation (with Schottky correction) [26, 27]

$$J_T(F,T) = A_{RLD}T^2 \exp\left(\frac{-\Phi + \sqrt{\frac{q^3F}{4\pi\epsilon_0}}}{k_BT}\right), \tag{2.5}$$

where J_T is the thermionic emission current density, F is the local electric field, T is temperature, Φ is the work function, $A_{RLD} = \frac{4\pi m k_B^2 q}{h_P^3}$ is Richardson's constant, m is the mass of an electron, k_B is the Boltzmann's constant, q is the elementary charge, h_P is the Planck's constant and ϵ_0 is the vacuum permittivity. Note that the barrier maximum in eq. 2.4 is $V_{\max} = \Phi - \sqrt{\frac{q^2 F}{4\pi\epsilon_0}}$.

Thermionic emission is the dominant contributing effect to emission current under relatively low field and high temperature conditions (see section 2.4).

2.3 Field emission

Under relatively low temperature and high field conditions (see section 2.4), the dominant electron emission effect is field emission. An analytical expression for the field emission can be found by assuming absolute zero temperature and approximating the tunnelling probability $D(U, F)$ (eq. 2.3) exponentially around the Fermi energy (Fowler-Nordheim approximation) [22] which gives the Fowler-Nordheim equation [15, 28]

$$J_{F0}(F) = \frac{aF^2}{\Phi\tau(F)^2} \exp\left(-\nu(F)\frac{b\Phi^{\frac{3}{2}}}{F}\right), \tag{2.6}$$

where $a = \frac{q^3}{8\pi h_P}$ and $b = \frac{8\pi\sqrt{2m}}{3qh_P}$ are the Fowler-Nordheim first and the second constant, respectively; τ and ν are correction factors, that depend on the shape of the metal surface energy barrier. For the Schottky-Nordheim barrier (eq. 2.4) [29]

$$\nu(F) \approx 1 - \frac{F}{F_b} + \frac{1}{6}\frac{F}{F_b}\ln\frac{F}{F_b} \tag{2.7}$$

and

$$\tau(F) \approx 1 + \frac{F}{9F_b}\left(1 - \frac{1}{2}\ln\frac{F}{F_b}\right), \tag{2.8}$$

where F_b is the critical electric field, which reduces the energy barrier with height Φ to zero. It is expressed as

$$F_b = \frac{4\pi\epsilon_0\Phi^2}{q^3}. \tag{2.9}$$

The equation 2.6 is known as the standard Fowler-Nordheim equation, which has been derived strictly for absolute zero temperature. In the case of non-zero temperature T, it must be multiplied by a temperature correction factor

$$J_F(F, T) = \Theta(F, T) J_{F0}(F). \tag{2.10}$$

The factor $\Theta(F, T)$ is given by [25]

$$\Theta(F, T) = \frac{\pi k_B T/d_T}{\sin(\pi k_B T/d_T)}, \tag{2.11}$$

where $d_T = \frac{2F}{3b\sqrt{\Phi}}$ is a parameter, which describes the lowering of the energy barrier.

The temperature corrected version of the Fowler-Nordheim equation (eq. 2.10) can not be applied when the field-temperature conditions go out of it's region of validity (see section 2.4), as some very non-physical effects can be introduced (such as electrons being absorbed into the protrusion). For a heating protrusion model, such as is studied in the current work, the conditions can easily go beyond the equation's validity. Thus, the standard Fowler-Nordheim equation (eq. 2.6) is used to estimate the field emission currents, as is traditionally done [12–14].

2.4 Applicability regions of emission equations

Richardson-Laue-Dushman (eq. 2.5) and Fowler-Nordheim (temperature corrected, eq. 2.10) emission equations have non-overlapping applicability regions [30]. Under high temperature and relatively low field conditions, the emission current is characterised by the Richardson's equation, and in low temperature and high field conditions, the current is characterised by Fowler-Nordheim equation (for copper see figure 2.2). Between the thermionic and field emission regions, there is the so-called transition or intermediate region, where neither of the two equations describe the current accurately.

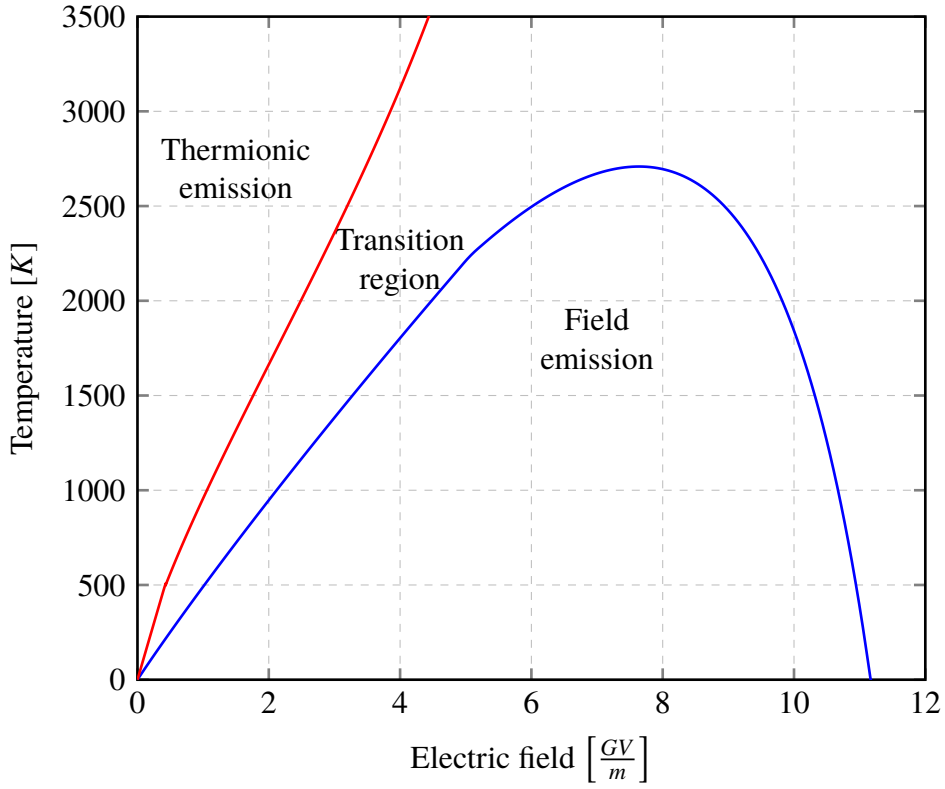

Figure 2.2: Applicability regions for Richardson's and Fowler-Nordheim (temperature corrected) equations for copper (work function $\Phi = 4.5eV$). Regions are defined based on [30].

3. Methodology

3.1 Simulated system

The studied system models the CLIC accelerating structure material under high external electric field. It consists of a single copper protrusion on the surface of an otherwise smooth copper cathode. The system is three dimensional and is symmetric about its central vertical axis. A cross section through the symmetrical axis can be seen in figure 3.1.

Most of the simulations are conducted by modelling a protrusion with a cylindrical base and a hemispherical cap on top. This simple geometry is also frequently used in other similar studies [11, 31] and allows for a comparison, if needed. The simulations were run with series of emitters with radii 1 nm, 2 nm, 3 nm and 4 nm. Two different values for height were chosen: 5 nm and 20 nm. Other shapes were also briefly studied, such as a protrusion with a conical base and hemispherical cap (see section 4.2 for the results). See table 3.1 for the studied geometries.

Three boundary value problems need to be solved. The first one is finding the electric field in the vacuum (section 3.2), the second is finding the electrical currents in copper (section 3.3) due to electron emission (see sections 2.2, 2.3 and 3.6). The third boundary value problem is finding the temperature distribution in the copper (see section 3.4). The corresponding boundary conditions can be also seen figure 3.1. The outer boundaries (i.e. the boundaries of the simulation box) need to be far enough that the boundaries don't influence the results near the protrusion. For a protrusion with height h, the top boundary was taken to be $20h$ away and the bottom boundary $7h$ away from the copper-vacuum boundary. The sides were $14h$ away from the protrusion sides. These distances were verified to not alter the solution near the emitter.

The partial differential equations are solved for the steady-state condition as the involved electrical and thermal processes reach the thermal equilibrium in time much shorter than the accessible experimental time scale (seconds) [32].

base	height [nm]	radiuses [nm]
cylindrical	5	1, 2, 3, 4
conical with 60° opening angle	5	1, 2, 3, 4
cylindrical	20	1, 2, 3, 4

Table 3.1: Studied geometries.

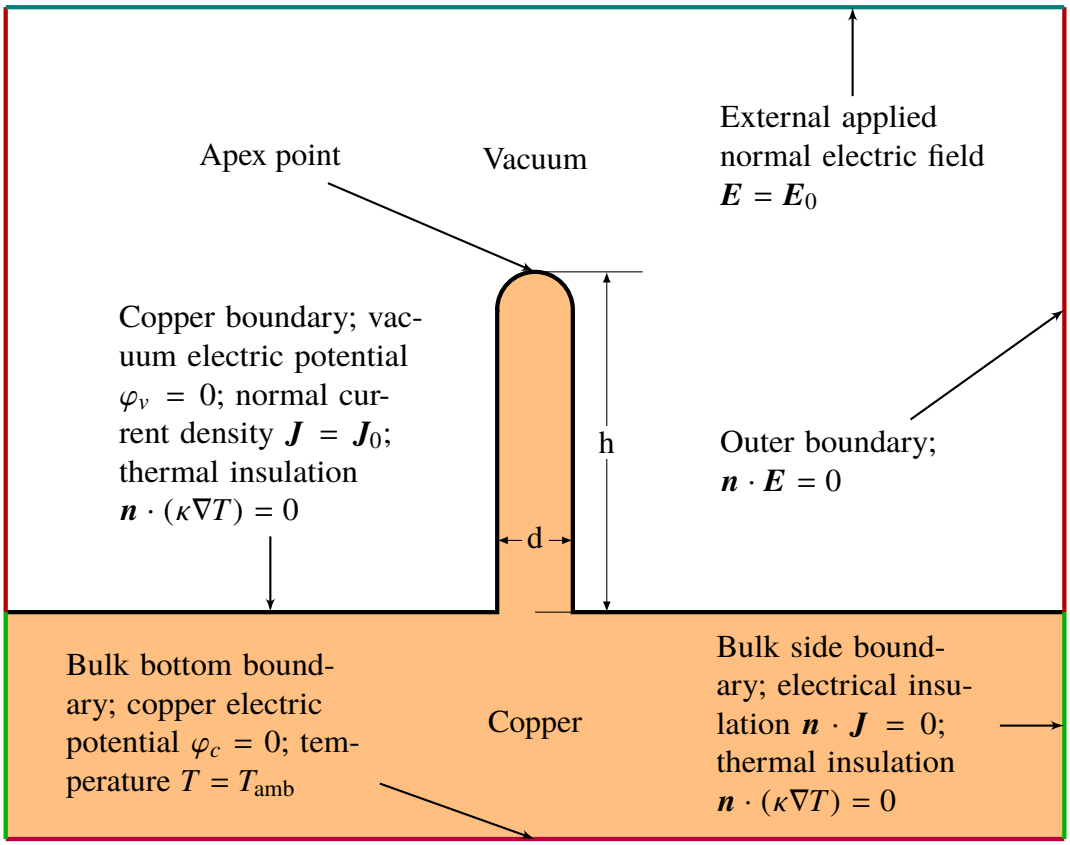

Figure 3.1: Schematic explaining the simulated system and boundary conditions (descriptions of boundary conditions are in the corresponding sections).

3.2 Electric field

In the simulated system (see figure 3.1), the electric field configuration corresponding to the boundary conditions needs to be found in the vacuum. The configuration also determines the field enhancement β.

The electric potential (and field) configuration in a system can be found by solving the *Poisson's equation*

$$\nabla^2 \varphi(\boldsymbol{r}) = -\frac{\rho(\boldsymbol{r})}{\epsilon_0}, \tag{3.1}$$

where $\varphi(\boldsymbol{r})$ is the electrostatic potential, $\rho(\boldsymbol{r})$ is the space charge density and ϵ_0 is the electric constant.

In the studied system, the emitted electrons from the protrusion will result in a negative space charge, reducing the electric field at the metal surface. This is called the space-charge screening effect [33, 34]. Even though at high currents and fields this effect should be considerable, it is ignored in this work. Thus, the space charge density is assumed to be $\rho(\boldsymbol{r}) = 0$ and the Poisson's equation takes the form of Laplace's equation

$$\nabla^2 \varphi(\boldsymbol{r}) = 0, \tag{3.2}$$

The Laplace's equation 3.2 has three different boundary conditions in the studied system (see figure 3.1). The top side of the simulation box has a Neumann boundary condition corresponding to the applied external electric field $\boldsymbol{E}_0$

$$-\nabla\varphi_v(\boldsymbol{r}) = \boldsymbol{E}(\boldsymbol{r}) = \boldsymbol{E}_0, \tag{3.3}$$

where $\varphi_v(\boldsymbol{r})$ is the potential in the vacuum[1] and $\boldsymbol{E}(\boldsymbol{r})$ is the electric field. The sides of the simulation box (vacuum boundary) have also a Neumann boundary condition

$$\boldsymbol{n} \cdot \big(-\nabla\varphi_v(\boldsymbol{r})\big) = \boldsymbol{n} \cdot \boldsymbol{E}(\boldsymbol{r}) = 0, \tag{3.4}$$

where $\boldsymbol{n}$ is the surface normal vector. This corresponds to an insulated boundary condition and if the simulation box is large enough, it does not affect the field configuration near the protrusion.

The copper-vacuum boundary has a Dirichlet boundary condition

$$\varphi_v(\boldsymbol{r}) = 0, \tag{3.5}$$

due to copper, as a conductive metal, having a constant potential over its surface [35].

3.3 Electric currents

3.3.1 Equation for electric currents

The electric currents will be found in the copper part of the system (see figure 3.1). The stationary differential equation for finding the potential corresponding to currents can be derived by combining the continuity equation with the differential Ohm's law and it can be represented as

$$\nabla \cdot (\sigma\nabla\varphi) = 0, \tag{3.6}$$

where $\sigma = \sigma(x, T)$ is the conductivity[2] and φ is the electric potential. And the current density $\boldsymbol{J}$ can be found by the differential Ohm's law

$$\boldsymbol{J} = \sigma\boldsymbol{E} = \sigma\nabla\varphi. \tag{3.7}$$

The equation 3.6 has three different boundary conditions in the system (see figure 3.1.). The first one is a Neumann boundary condition that corresponds to the electron emission current

$$\boldsymbol{J} = \sigma\nabla\varphi_c = \boldsymbol{J}_0(\boldsymbol{E}, T), \tag{3.8}$$

[1]The difference between vacuum and copper potential must be denoted, as they are solved in different domains for different PDE's.

[2]Spatial dependence comes from the nanoscale size effects, see section 3.5

where $\boldsymbol{J}$ is the current density, φ_c is the electric potential in copper and $\boldsymbol{J}_0(\boldsymbol{E}, T)$ is the emission current, which is generally dependent on the local electric field $\boldsymbol{E}$ and the temperature T (see sections 2.2, 2.3 and 3.6).

The bulk sides have a Neumann boundary condition corresponding to electrical insulation

$$\boldsymbol{n} \cdot \boldsymbol{J} = \boldsymbol{n} \cdot (\sigma \nabla \varphi_c) = 0, \tag{3.9}$$

where $\boldsymbol{n}$ is the surface normal vector of the boundary.

The bottom of the bulk has a Dirichlet boundary condition corresponding to a constant electric potential

$$\varphi_c = 0. \tag{3.10}$$

3.3.2 Electrical conductivity

The temperature dependence of the resistivity of copper $\rho(T)$ (and thus the electrical conductivity $\sigma(T) = \frac{1}{\rho(T)}$) can be accurately described by an equation developed by Matula [36] and improved by Schuster et al. [37], which is of the form

$$\rho(T) = A \left[1 + \frac{BT}{\theta - CT} + D \left(\frac{\theta - CT}{T} \right)^p \right] \Phi \left(\frac{\theta - CT}{T} \right) + \rho_0, \tag{3.11}$$

where θ, A, B, C, D, p, ρ_R are constants and

$$\Phi(x) = \frac{4}{x^5} \int_0^x \frac{z^5 e^z}{(e^z - 1)^2} dz. \tag{3.12}$$

This form is developed from Boltzmann transport theory and is widely used to model the resistivity of pure metals over wide ranges of temperatures. The values of the constants can be found by fitting equation 3.11 to experimental data. According to Schuster et al. [37], the best fit is achieved with the following values[3]

$$\begin{aligned} A &= 1.816013 \times 10^{-8} \Omega m, \\ B &= -2.404851 \times 10^{-3}, \\ C &= 4.560643 \times 10^{-2}, \\ D &= -5.976831 \times 10^{-3}, \\ p &= 1.838419, \\ \theta &= 310.8 K, \\ \rho_R &= 1.803751 \times 10^{-12} \Omega m. \end{aligned} \tag{3.13}$$

[3]Some of the values in the main part of the article [37] are incorrect, the correct values can be found in the appendix of the same article and additionally the minus in front of p was omitted to achieve matching results with the article's numerical data.

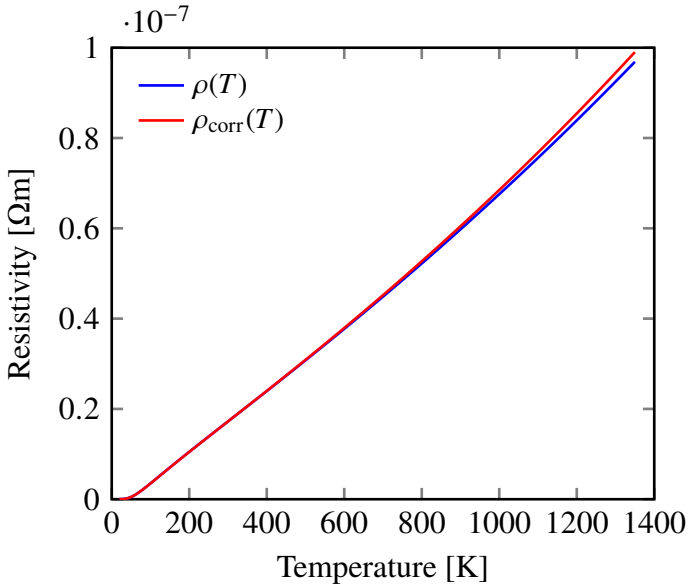

Figure 3.2: The temperature dependence of the resistivity of copper. $\rho(T)$ does not take thermal expansion into account and $\rho_{\text{corr}}(T)$ does.

Equation 3.11 is most accurate (and has been fitted) for the temperature range of 20 K to 1200 K but it is mentioned that it also works fairly well up until the melting point (1357.6 K). The result can be seen on figure 3.2.

Schuster et al. also found a small correction factor to the resistivity due to thermal expansion [37], which can be expressed as

$$\rho_{\text{corr}}(T) = \rho(T)\left(1 + \frac{\Delta L}{L_0}\right), \tag{3.14}$$

where $\frac{\Delta L}{L_0}$ is the linear thermal expansion coefficient and was found from table 12R in [38]. Nevertheless, the model of the current work does not consider thermal expansion and thus the correction factor is ignored (and as seen in figure 3.2, the difference is not very significant).

To use the resistivity data in computer simulations, the equation 3.11 can not be used as the calculation is computationally intensive. In that case tabulated data and linear interpolation of $\log_e \rho(T)$ versus $\log_e T$ should be used.

3.4 Heating

3.4.1 Heat equation

The temperature distribution can be found using the stationary (i.e. steady state) heat equation

$$-\nabla \cdot (\kappa \nabla T) = \rho J^2, \tag{3.15}$$

where $\kappa = \kappa(x, T)$ is the thermal conductivity, T is the temperature, $\rho = \rho(x, T)$ is the resistivity and J is the current density. The right side of equation 3.15 represents the volumetric resistive heating.

In the system, the heat equation (3.15) has two different boundary conditions (see figure 3.1). The copper-vacuum boundary and the copper bulk side boundary have the Neumann boundary condition corresponding to thermal insulation (thermal radiation is negligible [32])

$$\boldsymbol{n} \cdot (\kappa \nabla T) = 0, \tag{3.16}$$

where $\boldsymbol{n}$ is the surface normal vector. The bulk bottom boundary has the Dirichlet condition

$$T = T_{\text{amb}}, \tag{3.17}$$

where T_{amb} is the temperature of outer environment (i.e. the ambient temperature; usually $T_{\text{amb}} = 300\,\text{K}$).

3.4.2 Thermal conductivity

The thermal conductivity of a material depends on two effects: the lattice thermal conduction, caused by interatomic interactions and the electronic thermal conduction, caused by electronic effects. In copper (and most metals), the lattice thermal conduction is negligible compared to the electronic thermal conduction [39], and thus it is ignored in this work (but it is implicitly taken into account in HELMOD, which is discussed in section 3.10). The electronic component of the thermal conductivity can be calculated by the Wiedemann-Franz law [40]

$$\kappa(T) = LT\sigma(T), \tag{3.18}$$

where T is the temperature, $\sigma(T)$ is the electrical conductivity (found by 3.11) and $L = 2.443 \times 10^{-8} W\Omega K^{-2}$ is the Lorenz number.

The Wiedemann-Franz law is known to be not applicable under certain intermediate temperature conditions. The law was found to be valid for copper films above the temperature of 200 K [41]. The system in this work is studied above 200 K and thus the law is applicable in the range of temperatures relevant to this work.

3.5 Nanoscale size effects

In a large enough bulk material, the mean free path of electrons is mainly determined by electron-phonon and electron-defect scattering, as electron-electron and electron-boundary scattering are negligible. When the characteristic length, such as the diameter of the protrusion on copper surface or the size of grains (for a polycrystalline solid), is comparable with the bulk

mean free path of electrons, boundary scattering becomes important. Subsequently, the electrical conductivity σ and the thermal conductivity κ become size dependent. [42, pp. 174-182]

The size dependence is usually characterized by the Knudsen number $K_n = \lambda_b/d$, where λ_b is the bulk mean free path of electrons and d is the characteristic length (e.g. the diameter of a protrusion). The size dependent electrical and thermal conductivities can be expressed as

$$\begin{aligned} \sigma_{nano} &= F(K_n) \cdot \sigma_b, \\ \kappa_{nano} &= F(K_n) \cdot \kappa_b, \end{aligned} \tag{3.19}$$

where σ_b and κ_b are the bulk conductivities. The finite size effects correction factor $F(K_n)$ for a thin cylindrical wire can be found using [42, p. 182]

$$\begin{aligned} F(K_n) &= 1 - \frac{12(1-p)^2}{\pi} \sum_{m=1}^{\infty} m p^{m-1} G(K_n, m), \\ G(K_n, m) &= \int_0^1 \sqrt{1-\xi^2} \int_1^{\infty} \exp\left(-\frac{m\xi t}{K_n}\right) \frac{\sqrt{t^2-1}}{t^4} dt d\xi, \end{aligned} \tag{3.20}$$

where p is the specularity, which is defined as the probability that a boundary scattering event is elastic and specular and it depends on the surface roughness.

Asymptotic approximations for 3.20 are [43]

$$\text{for } K_n \ll 1: \quad F(K_n) \approx 1 - \frac{3K_n}{4}(1-p) + \frac{3K_n^3}{8}(1-p)^2 \sum_{v=1}^{\infty} \frac{p^{v-1}}{v^2}, \tag{3.21}$$

$$\begin{aligned} \text{for } K_n \gg 1: \quad F(K_n) \approx & \frac{1+p}{1-p}\frac{1}{K_n} - \frac{3}{8K_n^2}\left[\frac{1+4p+p^2}{(1-p)^2}(\ln(K_n) + 1.059)\right. \\ & \left. -(1-p)^2 \sum_{v=1}^{\infty} (v^3 p^{v-1} \ln v)\right] - \frac{2}{15K_n^3}\frac{(1+11p+11p^2+p^3)}{(1-p)^3}. \end{aligned} \tag{3.22}$$

The factor $F(K_n)$ can also be calculated using a simulation program by Yarimbiyik et al. [44, 45]. The simulation program calculates the effective conductances for thin film and line interconnections with a rectangular cross-sectional surface area and takes the dimensions of the system, grain structure and specularity as input.

The specularity value p for copper has been taken to be 0.01 in this work, which is close to the values reported in literature [46–48].

The Lorenz number L from the Wiedemann-Franz law (equation 3.18) also has a finite size dependence [49], due to phonon conductivity of copper becoming more important as the finite size decreases. This effect is very small and thus is ignored in this work [49].

3.6 General thermal field emission

Jensen et al. have developed an analytical equation, the general thermal field (GTF) emission equation, which describes the emission current in the transition region and also in the thermionic and field regions [17, 18]. It combines both, the Richardson-Laue-Dushman (eq. 2.5) and Fowler-Nordheim (eq. 2.6) equations as the limits at high temperatures and high electric fields, respectively. It is expressed as[4]

$$\begin{aligned} J_{GTF}(F_e, T) &= A_{RLD} T^2 N \left(\frac{\beta_T}{\beta_F(U_m)}, \beta_F(U_m)(U_o - \mu) \right), \\ N(n, s) &\approx n^2 \Sigma \left(\frac{1}{n} \right) e^{-s} + \Sigma(n) e^{-ns}, \end{aligned} \tag{3.23}$$

where J_{GTF} is the current density, F_e is the product of local electric field and elementary charge, T is temperature, A_{RLD} is the Richardson's constant (see equation 2.5), $\beta_T = \frac{1}{k_B T}$ is the thermal emission energy slope factor, $\beta_F(U_m)$ field emission energy slope factor, U_m and U_o are energy parameters discussed later, μ is the chemical potential (fermi level) and $\Sigma(x)$ is a function characteristic to the equation. $\Sigma(x)$ has been approximated in [17, p. 7] with the equation:

$$\Sigma(x) \approx \frac{1}{1-x} - x(1+x) + \frac{1}{4} x^3 (7x - 3) + \zeta(2) x^2 (1 - x^2), \tag{3.24}$$

where $\zeta(x)$ is the Riemann zeta function. $\Sigma(n)$ experiences a discontinuity at $n = 1$ but the function $N(n, s)$ (from equation 3.23) remains finite, as

$$\lim_{n \to 1} N(n, s) = e^{-s}(1 + s). \tag{3.25}$$

β_F can be calculated with the equation (43) in reference [17]

$$\beta_F(U) \approx \frac{1}{\phi} [B_q z + C_{FN}(1 - z) + 3(2B_{FN} - B_q - C_{FN}) z(1 - z)], \tag{3.26}$$

where the expressions of relevant parameters are in table 3.2 and used constants are in table 3.3.

In the general thermal field equation 3.23, $\beta_F(U)$ is always evaluated at U_m. U_m is an energy parameter, which depends on the emission regime (see table I in [17]) and can be found by

$$U_m = \mu + \phi, \qquad \text{when } T > T_{max} \tag{3.27}$$

$$\beta_F(U_m) = \beta_T, \qquad \text{when } T_{min} \leq T \leq T_{max} \tag{3.28}$$

$$U_m = \mu, \qquad \text{when } T < T_{min}, \tag{3.29}$$

[4]The following notation differences with [17, 18] were made: F_e instead of F and U instead of E.

Parameter	Description	Equation or page in [17]
$z = \frac{U-\mu}{\phi}$	-	p. 6
$B_q = C_q = \frac{\pi}{\hbar}\phi\sqrt{2m}\left(\frac{Q}{F_e^3}\right)^{1/4}$	-	(41)
$B_{FN} = \frac{4}{3\hbar F_e}\sqrt{2m\Phi^3}\nu(y)$	Fowler-Nordheim's B constant	(40)
$C_{FN} = \frac{2\phi}{\hbar F_e}\sqrt{2m\Phi}t(y)$ [a]	Fowler-Nordheim's C constant	(40)
$Q = \frac{q^2}{16\pi\epsilon_0}$	image potential factor	p. 6
$\phi = \Phi - \sqrt{4QF_e}$	potential barrier lowering	p. 6
$y = \frac{\sqrt{4QF_e}}{\Phi}$	barrier lowering parameter	p. 6
$\nu(y) \approx (1-y^2) + \frac{1}{3}y^2 ln(y)$	elliptical integral term (Forbes approx.)	(21)
$t(y) \approx \frac{1}{9}y^2(1-ln(y)) + 1$	elliptical integral term (Forbes approx.)	(23)
$\beta_T = \frac{1}{k_B T}$	thermal emission energy slope factor	-

Table 3.2: Expressions and descriptions for parameters used in the general thermal field equation. All of them are taken from reference [17].

[a] There was an error in [17], see [50, p. 46] equation (30).

where

$$T_{min} = \frac{1}{k_B \beta_F(\mu)} \tag{3.30}$$

$$T_{max} = \frac{1}{k_B \beta_F(\mu+\phi)}. \tag{3.31}$$

The equation 3.28 is a quadratic equation, whose greater[5] root is the correct U_m. From equation 3.26 then

$$[-3(2B_{FN} - B_q - C_{FN})]z_m^2 + [3(2B_{FN} - B_q - C_{FN}) + B_q - C_{FN}]z_m + [C_{FN} - \phi\beta_T] = 0. \tag{3.32}$$

[5] Reference [17, p. 7] states that the smaller root is the correct one, but the author of this work achieved matching results with [18] by using the greater root.

Constant	Description	Value
Φ	work function	$4.5eV$
μ	chemical potential (Fermi level)	$7eV$
q	elementary charge	$1.602\,176\,57 \times 10^{-19}C$
ϵ_0	electric constant	$1.418\,597\,23 \times 10^{-39}\frac{C^2}{eVnm}$
A_{RLD}	Richardson's constant	$120.17349\frac{A}{K^2cm^2}$
k_B	Boltzmann's constant	$\frac{1}{11604.506}\frac{eV}{K}$
m	mass of electron	$\frac{510998.9}{(2.997\,924\,58 \times 10^{17})^2}\frac{eV}{(nm/s)^2}$
$\hbar$	Planck's reduced constant	$6.582\,119\,28 \times 10^{-16}eVs$

Table 3.3: Relevant constants and their values.

Solving it for the z_m that corresponds to the greater root of U_m leads to

$$\begin{aligned} z_m &= \frac{-b}{2a} + \sqrt{\left(\frac{b}{2a}\right)^2 - \frac{c}{a}}, \\ a &= -3(2B_{FN} - B_q - C_{FN}), \\ b &= 6B_{FN} - 2B_q - 4C_{FN}, \\ c &= C_{FN} - \phi\beta_T. \end{aligned} \tag{3.33}$$

The ratio of energy slope factors $n = \frac{\beta_T}{\beta_F(U_m)}$ and the parameter $s = \beta_F(U_m)(U_o - \mu)$ can now be calculated by the following relations (see table I in [17]):

$$n = \begin{cases} \frac{\beta_T\phi}{B_q} & \text{when } T > T_{max} \\ 1.0 & \text{when } T_{min} \leq T \leq T_{max} \\ \frac{\beta_T\phi}{C_{FN}} & \text{when } T < T_{min}, \end{cases} \tag{3.34}$$

$$s = \begin{cases} B_q & \text{when } T > T_{max} \\ B_{FN} + \frac{b}{2}z_m^2 + \frac{2a}{3}z_m^3 & \text{when } T_{min} \leq T \leq T_{max} \\ B_{FN} & \text{when } T < T_{min}, \end{cases} \tag{3.35}$$

Using the previous two relations (3.34 and 3.35), the general thermal field equation 3.23 can be evaluated.

3.7 Fowler-Nordheim plot analysis

By assuming that the Fowler-Nordheim equation (eq. 2.6) holds, the field enhancement β on the surface of an electrode can be estimated by from the slope of $\ln(I/E^2)$ plotted against $1/E$, where I is the total measure current and E is the applied field [9, 13]. This method is frequently used by experimentalists.

By expressing the local electric field in eq. (2.6)[6] as $F = \beta E$, where E is the applied field and by integrating both sides over the emission area, we get

$$\frac{I}{E^2} = \frac{a}{\Phi} \int \beta^2 \exp\left(-\frac{b\Phi^{3/2}}{\beta E}\right) dS. \tag{3.36}$$

By introducing β_c (the average, or effective field enhancement) such that

$$\int \beta^2 \exp\left(-\frac{b\Phi^{3/2}}{\beta E}\right) dS = \beta_c^2 \exp\left(-\frac{b\Phi^{3/2}}{\beta_c E}\right) S, \tag{3.37}$$

and taking the logarithm of equation 3.36, we get

$$\ln\left(\frac{I}{E^2}\right) = -\frac{b\Phi^{3/2}}{\beta_c}\frac{1}{E} + \ln\left(\frac{a}{\Phi}\beta_c^2 S\right). \tag{3.38}$$

It can be seen from eq. 3.38, that the slope γ of $\ln\left(\frac{I}{E^2}\right)$ versus $\frac{1}{E}$, can be used to find the average field enhancement:

$$\beta_c = -\frac{b\Phi^{3/2}}{\gamma} \approx -\frac{65207}{\gamma}. \tag{3.39}$$

β_c is considered a good estimation to the real (maximum) β under the conditions that this work studies [9, 13]. This will be verified in the results section 4.6.

3.8 Finite element method

3.8.1 General overview

The finite element method (FEM) [51–55] is a numerical technique used to solve boundary value problems for differential equations. The method is used by first constructing a geometric model of the system and then dividing it into non-overlapping simple shaped subdomains or *elements* (which constitute the *mesh* and are composed by a number of *nodes*). Each element will have shape functions defined on them and with the use of variational calculus, the solved PDE can be approximated to an algebraic (steady state) or an ordinary differential (transient) equation within the element, where the unknowns are the sought values in the nodes. All the element equations together with the boundary conditions can be formulated into a matrix equation, which can be solved by numerical methods resulting in the sought values in the nodes. Using the values at the nodes, interpolation (by using the shape functions) is used to approximate the solution inside the elements and thus the solution in the whole region is obtained.

In this work, the finite element method is used to solve the Laplace's equation for the electric field (equation 3.2), the equation for electric currents (equation 3.6) and the heat equation (equation 3.15).

[6]The factors τ and ν have been approximated to 1.

3.8.2 Mesh

The geometry of the solved problem is divided into small non-overlapping mesh elements, which can vary in size and shape. In parts of the simulation area, where less accuracy is needed, the elements can be larger, and in areas, which need high accuracy, the mesh can be denser. In 1D, the elements are intervals. In 2D, usually triangular or quadrilateral mesh elements are used. And 3D problems can be discretized using tetrahedral, hexahedral, prism of pyramidal mesh elements.

To construct the FEM system matrix equation, the solved variable u needs to be expressed inside the elements using the element's nodal values. This is achieved using shape functions or *basis functions* N_k, such that (for a 2D case)

$$u(x, y) = \sum_k U_k N_k(x, y), \tag{3.40}$$

where $u(x, y)$ is the solved variable inside the element, U_k is the sought variable in the nodal point k. The shape functions $N_k(x, y)$ can be linear, quadratic or higher order. Higher order shape functions are computationally more intensive to calculate, but they are also more accurate. If in the analysis of the problem, the derivative of u is needed, at least quadratic shape functions should be used (otherwise the derivative is constant inside an element).

The mesh must be carefully analysed for each individual problem to obtain accurate solutions and not waste computational resources unnecessarily. Additionally, to verify mesh-independence of the solution, mesh refinement studies are needed.

3.8.3 Damped Newton's method

To solve nonlinear problems, typically the damped Newton's method is used [56]. To solve a system of nonlinear equations

$$F(x) = 0, \tag{3.41}$$

where the x is the solution vector and $F(x)$ is the residual vector, the iteration step can be described as follows. Given the vector for the nth step x^n (x^0 is the initial guess),

$$F'(x^n)\delta x = -F(x^n), \tag{3.42}$$

$$x^{n+1} = x^n + \lambda \delta x, \tag{3.43}$$

$$F'(x^{n+1})E = -F(x^n), \tag{3.44}$$

where $F'(x)$ is the Jacobian matrix, $\delta x = x^{n+1} - x^n$, $0 \leq \lambda \leq 1$ is the damping factor and E is the error estimation. If relative error corresponding to E is larger than the previous step, λ is reduced and x^{n+1} is recomputed. The reduction of λ is repeated until the relative error corr. to E is smaller than the previous step or a minimum value is reached and the solving is

cancelled. When x^{n+1} is successfully computed, the solver proceeds with a new step. Note that the equations 3.43 and 3.44 are systems of linear equations, which are solved by using either a direct (e.g PARDISO [57–60] or MUMPS [61]) or an iterative solver.

The solution is reached, when the specified relative tolerance exceeds the relative error found using a user-specified weighted Euclidean norm (multiple choices) [56].

3.9 Simulation procedure

3.9.1 COMSOL Multiphysics

The FEM model, that solves the discussed boundary values problems and takes the discussed effects into account was constructed using the software package COMSOL Multiphysics [62]. To solve the Laplace's eq. 3.2, the physics module *Electrostatics* was used. The electric currents (eq. 3.6) were solved with the *Electric Currents* module and heat equation (eq. 3.15) with the *Heat Transfer in Solids* module.

3.9.2 Mesh details

To model the system studied in this work (see section 3.1), a triangular mesh was used. In all the domains, where the partial differential equations (3.1, 3.6 and 3.15) were solved, quadratic shape functions were used.

Due to the tip of the protrusion having the highest field enhancement, it has the highest electric potential gradients, highest emission currents and most heating. Thus the mesh needs to be most dense at the surface of the spherical cap of the protrusion. To find the sufficient mesh density (that results in a satisfactory accuracy without wasting computational resources), a mesh refinement simulation was run by varying the number of boundary elements on the protrusion's spherical cap. The mesh density in other domains was also verified to be sufficient. The total current (GTF model) emitted from the whole copper surface of the protrusion was chosen as the mesh convergence criterion. The results of the refinement study can be seen in section 4.1. The relative error criterion of a converged mesh was taken to be 0.1 % (as firstly, the effects that this work studies do not need higher precision and secondly, many physical effects that are not taken into account, such as space-charge screening (section 3.2), introduce a much larger error).

3.9.3 Solver details

As the solved problem is highly nonlinear (heating depends on the currents and emission currents depend on the temperature; also the thermal and electrical conductivities are temperature-dependent), a nonlinear solver must be used. In this work, the Comsol's segragated solver [56] was used and the dependent variables corresponding to the three different partial differential equation (Poisson, current and heat) were separated to three different segragated steps. In each

step, one iteration of the damped Newton's method (section 3.8.3) is performed until the solution converges. To solve the linear systems occurring in the Newton's method, the direct solver PARDISO was used. The relative tolerance (i.e. the Euclidean norm of the relative error vector limit under which solution is accepted) was 10^{-6}.

The initial conditions for the equations which solved for electric potential (Poisson and current) were taken to be $V = 0$ and the initial temperature (for the heat equation) was taken to be $T = T_{\text{amb}}$ (i.e. the ambient temperature).

Most simulations in this work were conducted using a parametric sweep over a range of electric fields. The solution to the previous step was used as the initial condition to the next. The parametric stepping method was based on BDF (backward differentiation formula) with pseudo time as parameter for selecting the applied electric fields.

3.10 HELMOD software

The behaviour of the nanoprotrusion for FEM model was also compared to results obtained using hybrid electrodynamics - molecular dynamics (ED-MD) simulations (conducted by Stefan Parviainen from University of Helsinki). The ED-MD simulations were performed with the HELMOD (hybrid electrodyhamics - molecular dynamics) code [35], which represents the protrusion to be consisting of discrete atoms. As the current work does not study mechanical effects, the atom positions were fixed for the simulations. To find the electric field, currents and temperature distributions, HELMOD uses the finite difference method (FDM). The mesh size has a fixed structure with the nodal distance being in the order of copper lattice constant (each atom roughly corresponds to one node). To find the emission currents, the GTF equation was implemented by following the documentation created in the current thesis.

The simulations were ran under similar conditions (applied field, shape and dimensions of the emitter). Due to HELMOD surface is consisting of discrete atoms, it is considerably rougher than the infinitely smooth FEM geometry. The smaller the geometries, the more pronounced this effect is.

This comparison helps to evaluate both (FEM and HELMOD) nanoprotrusion models.

4. Results and discussion

4.1 Mesh convergence

In figure 4.1, the mesh convergence study for the used mesh (described in section 3.9.2) is presented. As the studied phenomena depend mostly on the accuracy of the solution on the tip boundary of the emitter, the density of boundary elements was varied. n denotes the number of boundary elements over the whole spherical cap. The convergence criterion of the mesh was taken to be the relative error in the total current emitted compared to a very dense $n = 1500$ reference mesh. As can be seen, the sought accuracy of 0.1 % (green line) is achieved at $n \approx 300$. The height of the protrusion was $h = 5\,\mathrm{nm}$ and the applied field was $E_{appl} = 1.5\,\mathrm{GV/m}$. These parameters were chosen for the study, because most simulations in this work were done under similar conditions and with similar geometries (but the number of elements on the boundary also scales with size and thus is also applicable to geometries of different length scales). Thus, the mesh ($n \approx 300$) was used throughout this work.

4.2 Electric field, current and temperature distribution

The resulting field configuration and currents in the emitter (for a standard geometry used in this work) can be seen on figure 4.2a for the applied electric field of $1.5\,\mathrm{GV/m}$. The colormap in the vacuum shows the norm of the electric field. The left side of the emitter shows the distribution of the current density norm and right side shows the temperature distribution. The emitter was cylindrical with height $h = 5\,\mathrm{nm}$ and radius $r = 1\,\mathrm{nm}$. The used emission current model was GTF. As can be seen, the tip boundary of the emitter has the highest local electric field and also the highest emission currents. Due to the high currents, most heating occurs also at the tip.

The field enhancements β (in the apex point of the emitter; found by solving the Laplace equation, see section 3.2) for different cylindrical protrusions (see section 3.1 for studied geometries) can be seen in table 4.1.

Emitters with shapes different from the standard cylindrical protrusion were also studied. One protrusion with same height and tip curvature as on figure 4.2a can be seen on figure 4.2b. It has a conical frustum as the base, which slanted side is tangent to the spherical tip. The angle of the slanted side with respect to bulk copper surface normal was 30°. Compared to the cylindrical emitter, the conical one has slightly lower field enhancement (dependent on the side

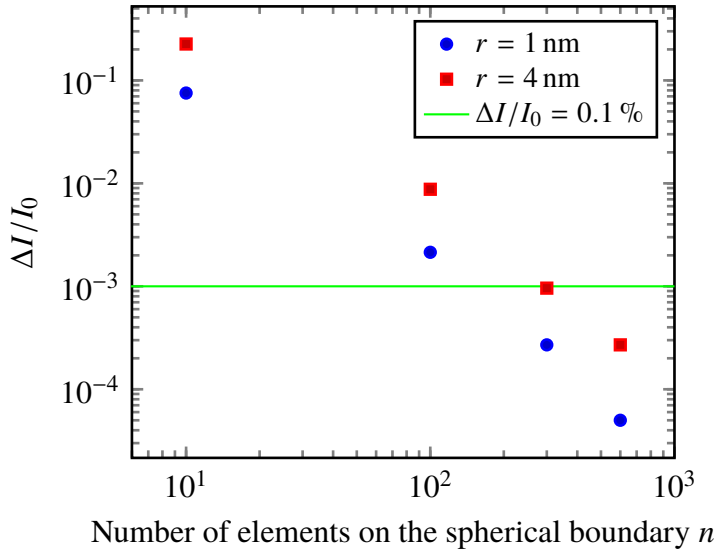

Figure 4.1: Mesh convergence. ΔI denotes the total current difference compared to a very dense ($n = 1500$) reference mesh. I_0 is the current found by the reference mesh. The green line corresponds to where the relative error of the total current is $10^{-3} = 0.1\%$. The height of the protrusion was $h = 5$ nm and the applied field was $E_{appl} = 1.5$ GV/m.

height \ radius	1 nm	2 nm	3 nm	4 nm
5 nm	7.28	4.76	3.82	3.32
20 nm	19.98	11.79	8.84	7.28

Table 4.1: Field enhancements at the apex point for cylindrical protrusions (cylindrical base with spherical cap on top). Found by solving the Laplace equation, see section 3.2.

angle) and also considerably greater electrical and thermal conduction occurring from the tip to the bulk. As a result, the temperature in the conical emitter is considerably lower than in a cylindrical emitter of the same height and tip curvature for the same applied electric field. The general behaviour is similar, but currents ramp up slightly later (mainly determined by local field) and temperature ramps up considerably later for the conical case. Additionally, the cylindrical protrusion is more widely used in other works and also easier to implement (e.g. in molecular dynamic simulations) and thus it is better for comparing to results obtained in other works in the field. Thus, from here on, the results of this work are achieved using the cylindrical shape.

4.3 Emission currents

Figure 4.3 shows the current density dependence on the local electric field of the Fowler-Nordheim (FN) (eq. 2.6), general thermal-field (GTF) (eq. 3.23) and Richardson-Laue-Dushman (RLD) equation (eq. 2.5). As can be seen, the GTF model converges to FN at high fields and to RLD at low fields. FN equation becomes very inaccurate at lower fields as it does not take into account the thermal contribution and even at higher fields (where GTF is in field emission regime

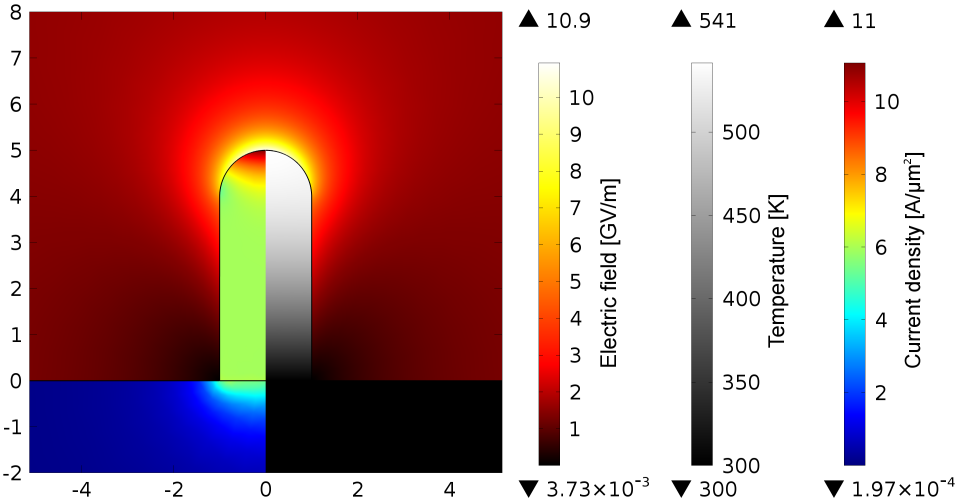

(a) Cylindrical protrusion (cylinder with a hemispherical cap).

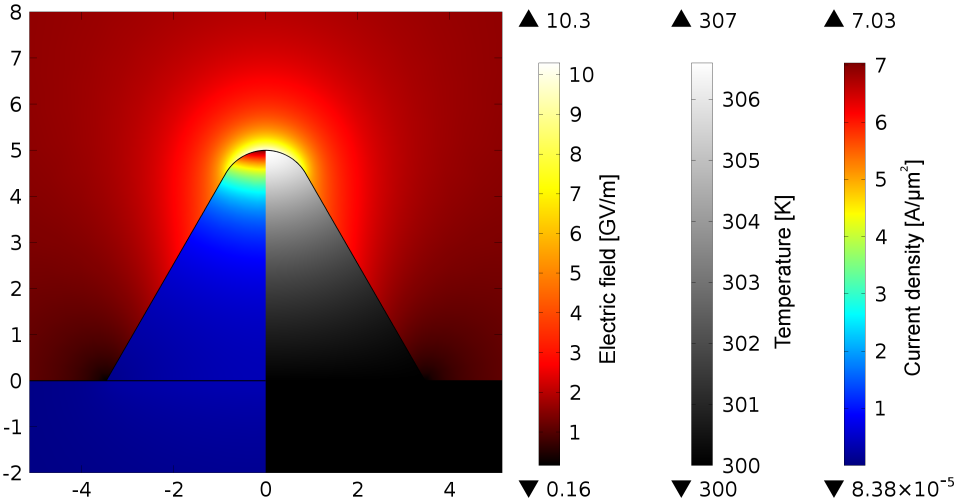

(b) Conical protrusion (conical frustum with a spherical cap, sides tangent to the sphere). Angle of the slanted side was 30°

Figure 4.2: Electric field, current and temperature distributions for the protrusions. In both cases, height was 5 nm, radius 1 nm, applied field 1.5 GV/m. The emission currents were found using the GTF model.

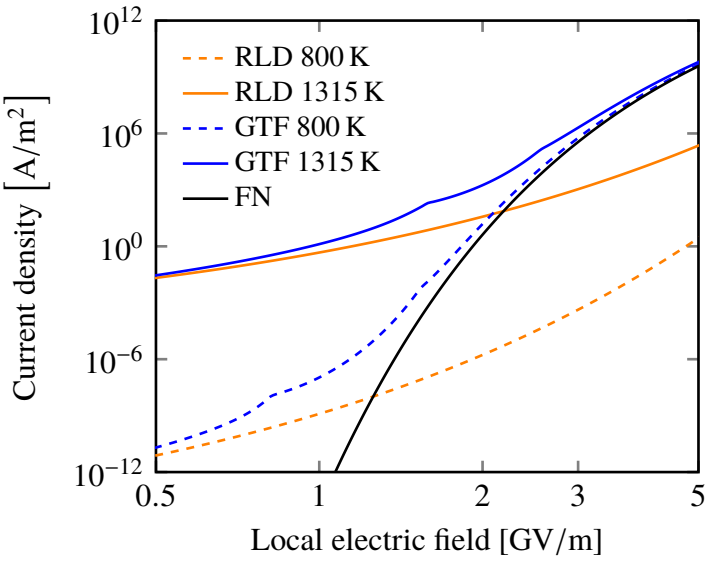

Figure 4.3: Current density dependence on local electric field for a constant temperature (copper). The figure shows how general thermal-field (GTF) current density compares to the Richardson's and Fowler-Nordheim (FN) currents.

(see section 3.6)), it gives slightly lower values than GTF. The figure 4.3 also verifies that the implementation (and documentation) of the GTF equation used in this work are correct.

The emission currents distribution can be seen on figure 4.4. As the tip apex has the highest local field and temperature, most of the current is emitted from there.

When ramping up the applied electric field, the system will develop equilibrium current and temperature distributions for each applied electric field value. The total emission current (GTF model) corresponding to the emerged field and temperature distributions versus the applied field can be seen on figure 4.5. The values are plotted until the melting point of the copper, as from that point onward, the resistivity model (section 3.3.2) breaks down and also the melted copper may lose it's shape. As can be seen on the figure, the smaller the radius of the emitter, the earlier total emitted current ramps up, which is to be expected, as the field enhancement is considerably higher for the narrower tips.

By observing closely the lines near the melting (cut-off) point on figure 4.5, the line turns practically vertical. This is due to a large part of the emitter being in the thermal emission region (meaning that thermal excitations are having a considerable effect on the emission current; see section 3.6) and the current that is heating the emitter is increased by the resulting temperature increase. This feedback loop can only end in the melting (and vaporization, leading to a breakdown) of the protrusion (see section 4.4 for thermal behaviour). The described effect is purely thermal and thus does not occur when using the Fowler-Nordheim emission model.

Figure 4.6 shows the proportion of FN current to the GTF current. At low fields, GTF dominates, as it takes into account the contribution from the thermal emission due to ambient temperature (see figure 4.7 to see the corresponding temperature for the applied field), but the currents are negligible and without practical importance (see figure 4.5) when no macroscopic

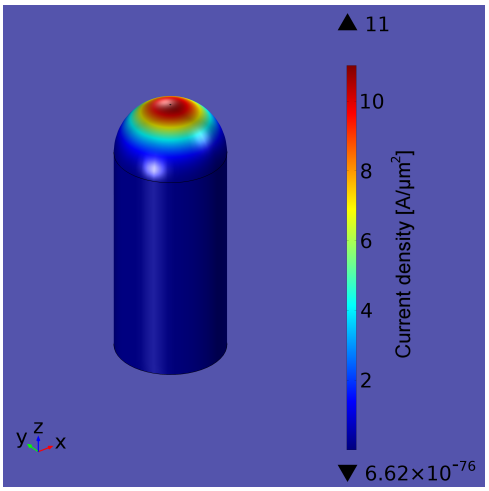

Figure 4.4: The emission current distribution on the emitter surface. Height was 5 nm, radius 1 nm, applied field 1.5 GV/m. The emission currents were found using the GTF model. Same conditions as in figure 4.2.

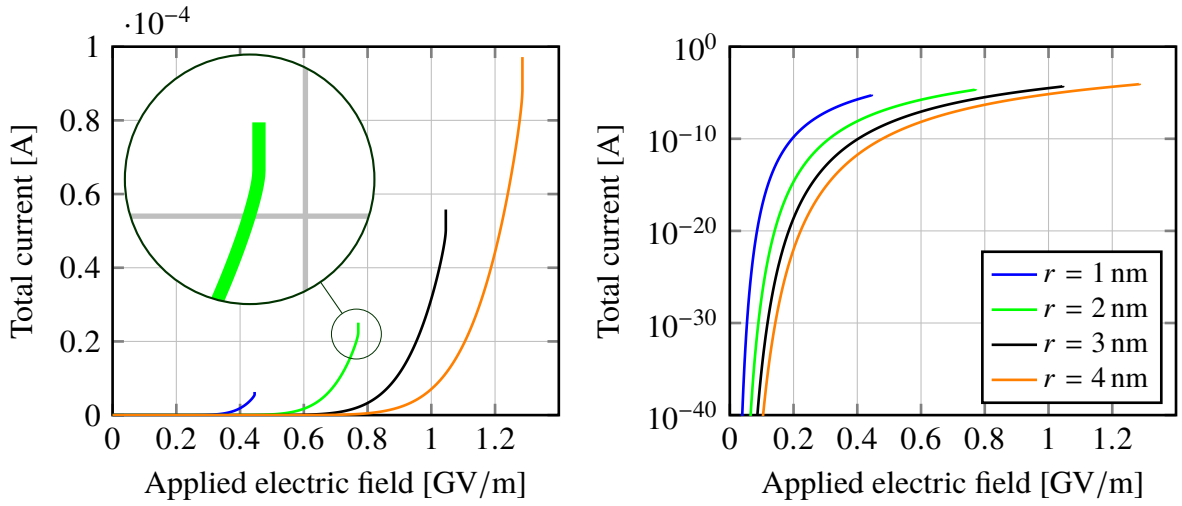

Figure 4.5: The total emission current versus the applied field in linear and logarithmic scale. The height of the emitters was $h = 20$ nm. The lines are cut when the tip temperature reaches the melting point.

heating has occurred (i.e. the ambient temperature is ~300 K). As the applied field increases, the field emission part of GTF current increases much more than the thermionic part (see equations 2.5 and 2.6 for the corresponding field dependences) and the total GTF current approaches the FN current. When the current reaches high enough to cause considerable temperature increase in the emitter, the thermal part of the current quickly grows and the GTF current deviates from FN current (over 15 % near the melting point, see fig 4.6).

4.4 Thermal behaviour

Figure 4.7 shows the dependence of the apex point temperature on the applied electric field. The lines are cut at the melting point, $T = 1357.6$ K. As can be seen, after some critical field

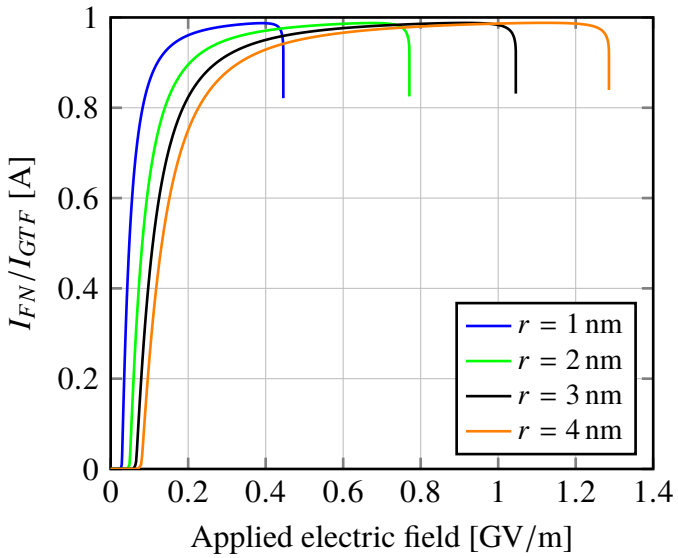

Figure 4.6: The total FN emission current divided by the GTF current versus the applied field. The height of the emitters was $h = 20\,\text{nm}$. The lines are cut when the tip temperature reaches the melting point.

r[nm]	ΔE[MV/m]	% of $E_{\text{melt, gtf}}$
1	5.56	1.25 %
2	9.54	1.24 %
3	12.84	1.23 %
4	15.69	1.22 %

Table 4.2: The difference in GTF and FN melting fields for the four emitters. See fig 4.7 for explanation of ΔE. Third column shows $\Delta E/E_{\text{melt, gtf}}$ in %, where $E_{\text{melt, gtf}}$ is the melting field corresponding to GTF. The height of the protrusion was $h = 20\,\text{nm}$.

value, the emitting tip starts to heat up very rapidly until it eventually melts. This behaviour is caused by the combined effects of thermionic emission, resistivity increase due to temperature rise and the exponential nature of the emission currents. The lines corresponding to the GTF model exhibit the same vertical line near the melting point as the currents, corresponding to the positive temperature-thermionic emission current feedback loop. The difference in the melting field values for GTF and FN model can be seen in table 4.2. The GTF protrusion melted for $\sim 1.2\,\%$ smaller field.

The melting field for the protrusions was highly dependent on the aspect ratio (h/r). It was $0.446\,\text{GV/m}$, $0.771\,\text{GV/m}$, $1.045\,\text{GV/m}$ and $1.286\,\text{GV/m}$ for the radii 1 nm, 2 nm, 3 nm and 4 nm, respectively, as seen on figure 4.7

Near the melting point, the temperature according to the FN model was $\sim 50\,\%$ of the GTF temperature, as seen on figure 4.8.

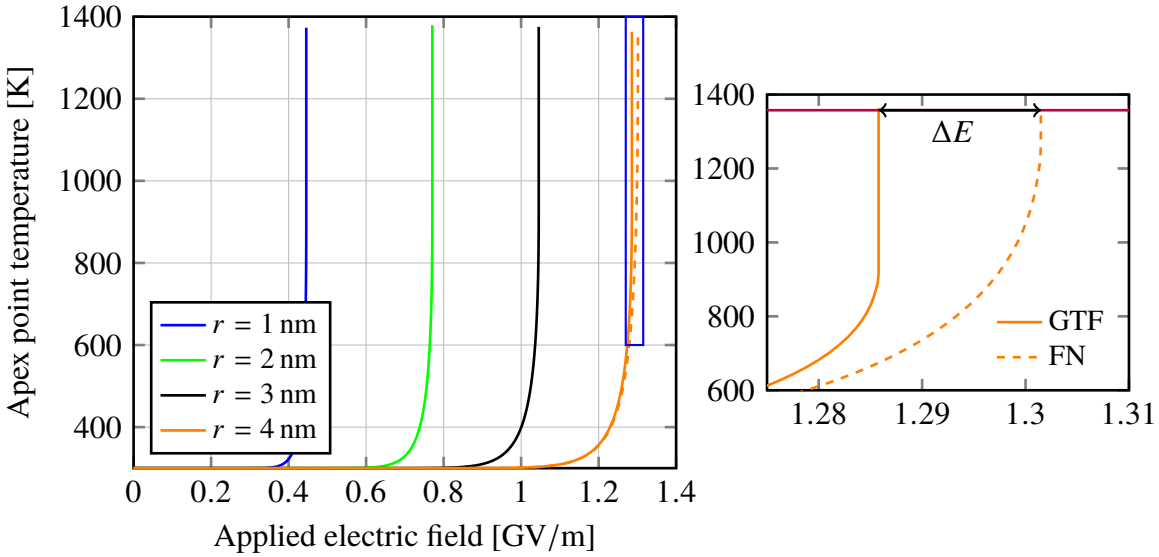

Figure 4.7: The apex point temperature dependence on the applied electric field. Protrusion height was $h = 20\,\text{nm}$. The right plot represents the magnified blue rectangle of left plot.

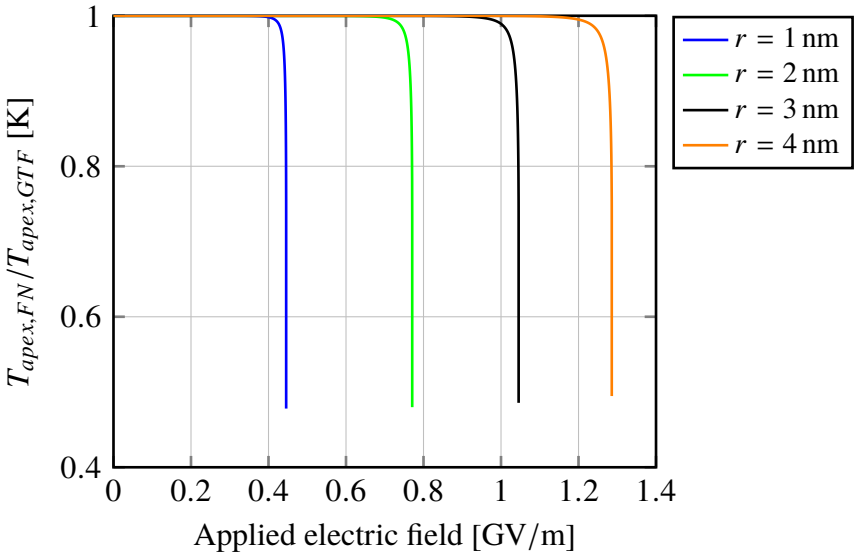

Figure 4.8: The temperature in the apex point for FN model divided by the temperature for GTF model versus the applied electric field. Protrusion height was $h = 20\,\text{nm}$.

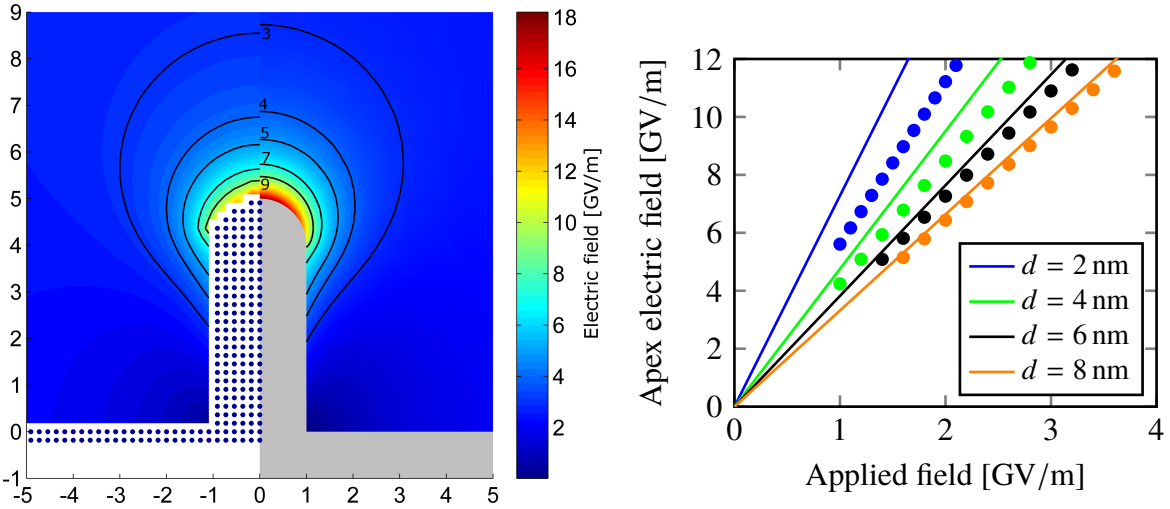

Figure 4.9: Left: HELMOD and FEM local electric field distributions. The applied field was $E_{\text{appl}} = 2.5\,\text{GV/m}$ and the protrusion dimensions were $h = 5\,\text{nm}$, $r = 1\,\text{nm}$. The electric field modulus was constant along the black lines. **Right:** The difference in the apex field between the FEM and HELMOD models. The continuous lines are FEM results, while dots are HELMOD. Considerable differences in field enhancement factors $\beta = E_{\text{apex}}/E_{\text{applied}}$ can be observed.

4.5 Comparison with HELMOD

The behaviour of the nanoprotrusion for the FEM model was also compared to results of hybrid electrodynamics - molecular dynamics (ED-MD) simulations (conducted by Stefan Parviainen from University of Helsinki) performed with the HELMOD [35] code. See section 3.10 for details about HELMOD.

Figure 4.9 shows the difference of the electric field distribution between the FEM and HELMOD models. As can be seen, the overall field distribution seems to match well, but due to fundamental differences in the representation of the metal surface, the field right at the surface is considerably lower for the HELMOD model (fig. 4.9 right plot). This can be also because the FDM grid had a fixed uniform structure with node distance in the order of copper lattice constant. In consequence, the other characteristics should be compared as a function of the apex electric field, not the applied field. This eliminates (to some degree) the discrepancy caused by field calculations.

The total emitted currents as a function of the apex field can be seen on figure 4.10. The general dependence is similar, but considerable differences can be observed. Even though the dependence is studied with respect to the apex field, the HELMOD surface is still considerably rougher. Additionally, the algorithms for finding currents and solving the heat equation inside the emitter are different (HELMOD approximates the emitter as a 1D structure).

The temperature dependence on the apex field can be seen on figure 4.11. Qualitatively, the behaviour is similar: rapid temperature increase until melting is observed after some critical field value. Quantitatively, the differences correspond to the current disparities discussed earlier.

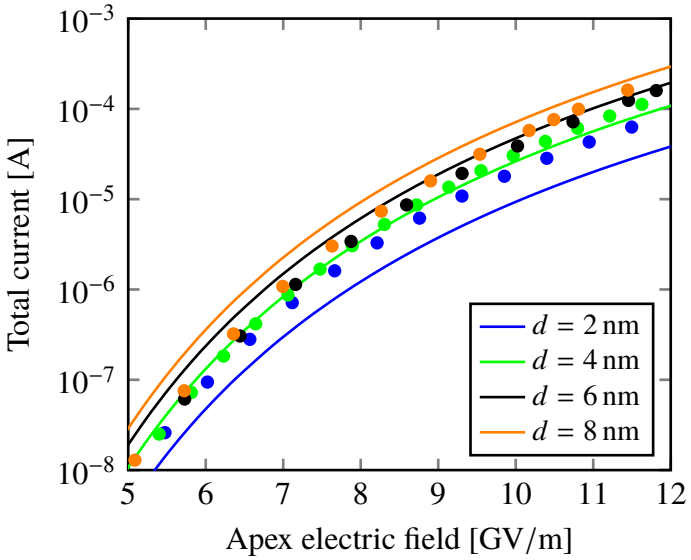

Figure 4.10: The total emitted current as a function of the apex electric field for FEM (continuous lines) and HELMOD (dots). Height of the protrusion was $h = 5\,\text{nm}$. Temperature was held constant throughout the simulation at $T = 300\,\text{K}$.

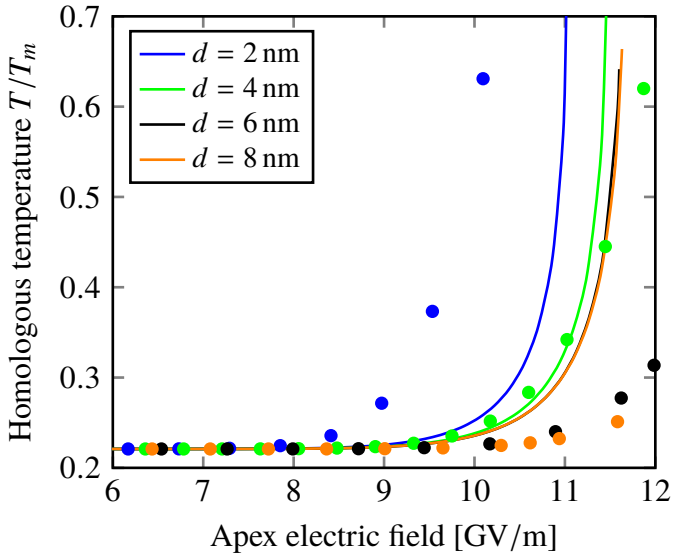

Figure 4.11: The temperature at the apex point divided by the melting temperature $T_m = 1357.6\,\text{K}$ as a function of the apex electric field for FEM (continuous lines) and HELMOD (dots). Height of the protrusion was $h = 5\,\text{nm}$.

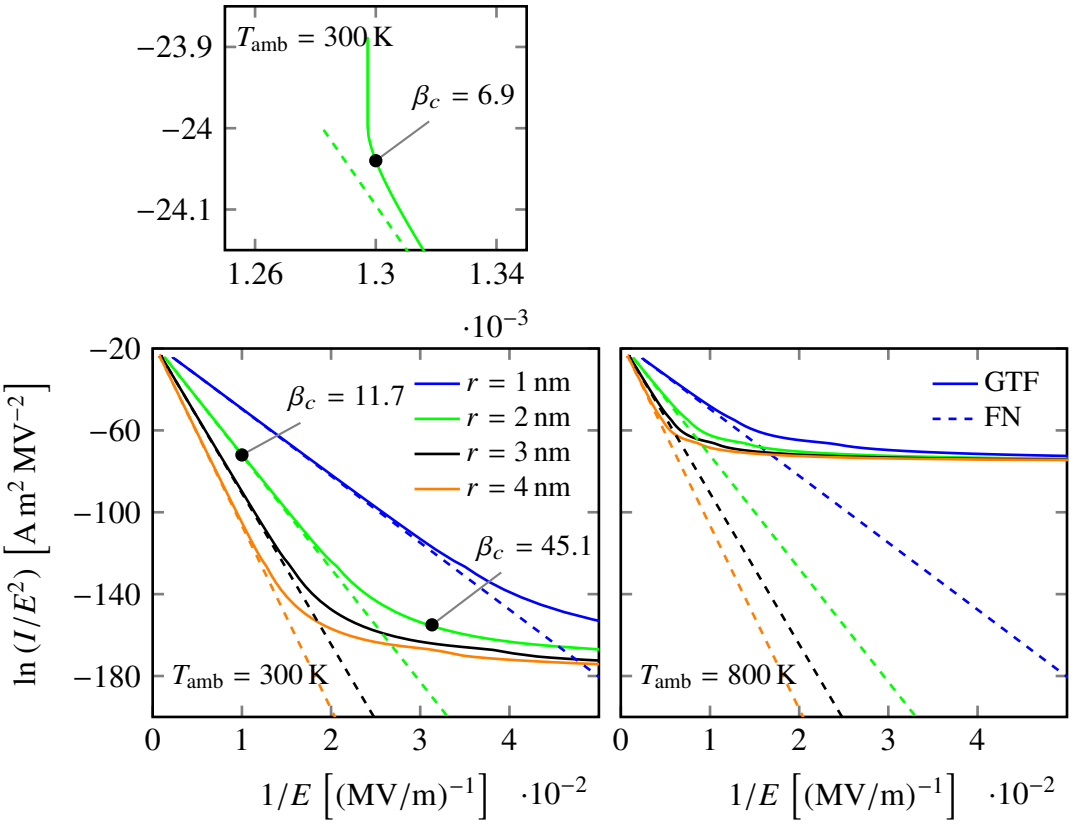

Figure 4.12: Fowler-Nordheim plot. The dashed lines correspond to the Fowler-Nordheim emission equation and the continuous lines to the general thermal-field equation. Protrusion height $h = 20\,\text{nm}$. Field enhancement in the apex point as found directly from the simulation is $\beta = 11.8$ for the $r = 2\,\text{nm}$ case. **Lower left:** the ambient temperature was $T_{\text{ambient}} = 300\,\text{K}$. **Upper left:** magnified part of the FN plot near melting point. **Lower right:** $T_{\text{ambient}} = 800\,\text{K}$.

4.6 Fowler-Nordheim plot

Experimentalists frequently use the FN plot to estimate the field enhancement β of the protrusions on an electrode. See section 3.7. However, this method assumes that the emission current obeys the Fowler-Nordheim equation (eq. 2.6) and does not take any thermal effects into account.

Figure 4.12 shows the Fowler-Nordheim plot. The dashed lines found using the Fowler-Nordheim equation are straight, as the theory predicts. The effective β_c found from the slope of those lines are in good accordance with the real β found directly from the simulation (see table 4.1). For the protrusion with dimensions $h = 20\,\text{nm}$, $r = 2\,\text{nm}$, the field enhancements are $\beta_c \approx 11.7$ and $\beta = 11.79$ and the difference is less than 1 %. Similar results can be found for other geometries. Thus the claim at the end of section 3.7, that $\beta_c \approx \beta$, has been verified (under the assumption that emission currents are characterized by the FN equation).

The continuous lines of figure 4.12 were found using the GTF emission model. At high fields, the GTF lines coincide with the FN lines, as expected (due to field emission dominating in the GTF equation). Also the estimated field enhancements β_c coincide. At lower fields, however, where the thermionic part of the emission current becomes comparable or greater

than the field emission part, the GTF line deviates from the FN line. The slopes diverge and the β_c found using the FN plot analysis, overestimates the field enhancement. The lower the field, the bigger the overestimation (β_c can grow arbitrarily large). In the figure 4.12, where the ambient temperature (see figure 3.1) is $T_{\text{ambient}} = 300\,\text{K}$, deviation between GTF and FN occurs at practically unmeasurable currents, but when the temperature raises macroscopically (due to emission currents, breakdowns, induction currents or something else), the deviation occurs at much higher fields and currents (see fig 4.12 where the $T_{\text{ambient}} = 800\,\text{K}$). Similar slope behaviour to the GTF lines has also been detected by experiments [63].

Near the melting point of the protrusion, the GTF lines deviate from FN once again (see the magnified part of figure 4.12). This is caused by the thermionic component of the GTF current rising in accordance to the temperature rise. And the vertical part (corresponding to the feedback loop, discussed earlier) is also present. In this region, the FN plot analysis method underestimates the field enhancement, becoming close to zero at the end.

5. Conclusions and future directions

5.1 Conclusions

The the objective of this work, to investigate the electric currents and thermal behaviour of the copper nanoprotrusion using the GTF emission model was fulfilled. The results corresponding to the posed sub-objectives of the work (section 1.2) follow.

- A straightforward mathematical implementation of the GTF equation was created.
- The electric currents and the thermal behaviour of the FEM nanoprotrusion model was studied for a range of applied field values until the protrusion reached the melting temperature. The electric field was most enhanced at the tip apex and that point also had the highest currents and heating. The total emission current for the studied protrusions ($h = 20\,\text{nm}$, $r = 1\,\text{nm}$ to $4\,\text{nm}$) was in the order of 10^{-4}A near the melting point. The melting field for the protrusions was highly dependent on the aspect ratio of the protrusion, from $0.446\,\text{GV/m}$ to $1.286\,\text{GV/m}$ for the $r = 1\,\text{nm}$ and $r = 4\,\text{nm}$ case, respectively. The temperature behaviour was highly non-linear - after some critical applied field value, the temperature started to rise quickly until the melting temperature.
- The behaviour of the FEM system using the GTF emission model was also compared to the FN model. Near the melting point, the total emitted current found by the FN equation was over 15 % smaller. Additionally, the model using the FN equation reached the melting point for ~1.2 % lower field. The GTF temperature was up to ~50 % higher near the melting point.
- The thermal effects of the FN plot were also investigated. The FN plot for the GTF model demonstrates significant thermal deviations from the FN plot obtained with the FN model. At lower fields (especially, when some macroscopic heating has occurred beforehand) the field enhancement β_c estimated from the slope of the FN plot can grow arbitrarily large. Near the melting field of the protrusion, another thermal deviation is present, corresponding to the high melting temperature. This deviation, however, influences the estimated β_c to decrease (down to zero).
- The behaviour of the FEM nanoprotrusion model was also compared with the HELMOD model. Due to fundamental surface representation differences in FEM and MD, the

resulting surface field was considerably different. The total emission current and tip temperature had similar dependencies of the apex point electric field for both models, but also numerically considerable differences were present.

5.2 Future directions

Even though the GTF equation has been added to the FEM model and the accompanying effects have been analysed thoroughly in this work, there are numerous other effects to analyse that may have an non-negligible effect. A non-exhaustive list about physical phenomena, which should be investigated in conjunction with the current FEM nanoprotrusion model is as follows

- Nottingham effect - emitted electrons can cool or heat the protrusion, depending on their energy. When the energy is lower than Fermi level, the protrusion is heated, and when it's higher, the protrusion is cooled [18, 22, 64].
- The finite size effects (section 3.5) depend on temperature due to the mean free path of electrons depending on temperature.
- The space charge screening effect (described in section 3.2) reduces considerably the local field on the tip of the emitter [33]. This could also increase the proportion of thermionic emission, making the GTF equation even more important when compared to FN.
- Work function depends on the crystallographic orientation, which could considerably influence the emitted current.

Additionally, to understand the onset of breakdowns, the mechanical effects should also be studied. In addition to the electrostatic stress on the protrusion's surface, there occurs the magnetostatic stress (due to currents in the protrusion) and stress due to electromigration [65]. The effect of both of these stresses should be investigated.

Implementing the general thermal-field emission equation to the high electric field nanoprotrusion model

Kristjan Eimre

Summary

Many devices, such as the particle accelerator Compact Linear Collider (CLIC), that use strong electric fields experience vacuum discharges, which damage the devices or lower their performance. It has been speculated, that the electric discharges are initiated by nanoscale protrusions on the cathode surface, which emit currents and thus heat until vaporization. These protrusions have been studied by assuming that the emission currents obey the Fowler-Nordheim (FN) equation, which does not take the contribution of thermionic emission into account. This is often inaccurate as the protrusions reach high temperatures.

Jensen et al (JAP, 2007) developed an analytical model, the general thermal field (GTF) emission equation, that considers both emission phenomena, the field emission (characterized by the FN equation) and the thermionic emission (which is due to electrons being emitted due to thermal effects). One of the main results of the current thesis was to turn the theoretical concepts of Jensen into a straightforward mathematical implementation and provide a clear documentation about it.

The created implementation was also used in a finite element method (FEM) model of a nanoprotrusion on a copper cathode with a strong external electric field applied (striving to replicate the CLIC DC experiment conditions). Three different fully coupled boundary value problems were solved with FEM: the Laplace's equation to find the electric field distribution, electric currents inside the protrusion and the heat equation to find the temperature distribution corresponding to the currents (Joule heating). Nanoscale size effects, that decrease the electrical and thermal conductivities in nanoscale structures were also taken into account. The behaviour of the currents and temperatures as a function of applied electric field was studied. The results were also compared to equivalent simulations for which the Fowler-Nordheim equation was used to find the emission currents.

Different geometries of protrusions were studied, the main results were presented for protrusions with a cylindrical base and a hemispherical cap with a height of 20 nm and radiuses of 1 nm, 2 nm, 3 nm and 4 nm.

The melting field for the protrusions was highly dependent on the aspect ratio of the protrusion, from 0.446 GV/m to 1.286 GV/m for the height 20 nm and radius 1 nm to 4 nm. The total emission current was in the order of 10^{-4}A near the melting point.

The total emission current found with FN equation was ~15 % lower near the melting point. The model utilizing GTF reaches melting temperature at about ~1.2 % lower field compared to FN. The GTF temperature is up to ~50 % higher near the melting point.

The thermal and current behaviour of the FEM nanoprotrusion model was also compared with a hybrid electrodynamics - molecular dynamics (ED-MD) model (using the HELMOD code). Due to fundamental surface representation differences in FEM and MD, the resulting surface field was considerably different. The total emission current and tip temperature had similar dependencies of the apex point electric field for both models, but also numerically considerable discrepancies were present, as was expected.

The Fowler-Nordheim plot is a way to express macroscopic current and field measurements such that the field enhancement β can be estimated from the slope of the plot. This estimation of β assumes that the emission currents obey the FN equation and no thermionic current is present. Under the GTF model, FN plot exhibits significant thermal deviations near lower field (especially, when some macroscopic heating has occurred beforehand). The field enhancement β_c estimated from the slope of the FN plot can grow arbitrarily large in the deviated part. Near the melting field of the protrusion, another thermal deviation is present, corresponding to the high melting temperature. This deviation, however, influences the estimated β_c to decrease (down to zero).

Üldise termo- ja väljaemissiooni võrrandi implementeerimine kõrges elektriväljas nanoteraviku mudelile

Kristjan Eimre

Kokkuvõte

Paljudes tänapäeva seadmetes, kus kasutatakse kõrgeid elektrivälju, esinevad elektrilised läbilöögid, mis kahjustavad seadmeid. CERN-is planeeritavas osakeste kiirendis Kompaktses Lineaarpõrgutis (CLIC) on läbilöökide kontrolli alla saamine otsustavad tähtsusega. Arvatakse, et läbilöökide põhjusteks on elektroodide pinnal olevad nanoskaalas teravikud, kus on rakendatud väli oluliselt võimendunud. Võimendunud välja tõttu on teravikest väljuv emissioonivool samuti kõrgem, mis soojendab (Joule'i-Lenzi seadus) teravikke kuni aurustumiseni. Seda protsessi on varem uuritud eeldades, et emissioonivoolud alluvad Fowler-Nordheimi (FN) võrrandile, mis ei arvesta termoemissiooni vooludega. See on aga ebatäpne, kuna antud protsessis saavutavad teravikud kõrgeid temperatuure.

Jensen et al (JAP, 2007) arendas välja üldise termo- ja väljaemissiooni (GTF) võrrandi, mis arvestab nii elektronide tunnelleerumisega (väljaemissioon) kui ka termiliste ergastuste poolt põhjustatud elektronide emissiooniga. Üks peamisi antud töö tulemusi oli Jenseni teoreetiliste ideede põhjal luua matemaatiline GTF võrrandi implementatsioon ja see selgelt dokumenteerida.

Antud töö raames implementeeriti GTF võrrand ka lõplike elementide meetodil (FEM) põhinevasse nanoteraviku mudelisse. FEM mudel kujutas vasest katoodi ja vaakumi piirpinnal asuvat nanoteravikku, millele rakendati kõrge elektriväli (üritades imiteerida CLIC'i tingimusi). Lõplike elementide meetodiga lahendati kolme erinevat äärevääartusprobleemi: Laplace'i võrrandit vaakumis elektrivälja jaotuse saamiseks; elektrivoolude võrrandit vases; ja soojuslevivõrrandit vases. Samuti arvestati nanoskaala efektidega, mis vähendasid teravikus oluliselt elektri- ja soojusjuhtivust.

Mudeli käitumist uuriti erinevate geomeetriate puhul sõltuvalt rakendatud elektriväljast. Tulemusi võrreldi ka simulatsioonide tulemustega, mille puhul oli emisioonivoolude arvutamiseks kasutatud Fowler-Nordheimi võrrandit. Uuriti erinevaid geomeetriaid, kuid peamised tulemused esitati teraviku jaoks, millel oli silindrikujuline alus koos poolsfäärikujuline tipuga ning mille kõrgus oli $h = 20\,\text{nm}$ ja raadiust varieeriti $1\,\text{nm}$ kuni $4\,\text{nm}$.

Elektrivälja võimendus oli teraviku tipus kõige suurem ja sealt eraldus ka kõige suurem emissioonivool ning toimus kõige intensiivsem soojenemine. Kogu teravikult emiteeritud vool saavutas sulamistemperatuuri lähedal väärtuse suurusjärgus 10^{-4}A. Kogu vool leitud FN võrrandiga lähenes rakendatud välja kasvamisel GTF voolule, ning kui vool sai piisavalt suureks, et oluliselt temperatuuri tõsta teravikus, hakkas GTF mudel andma suuremaid voolusid FN mudelist. Sulemustemperatuuri lähedal andis GTF mudel üle 15 % suuremat voolu.

Teraviku termilist käitumist iseloomustas oluline mittelineaarsus - kindla kriitilise rakendatud välja juures hakkas teraviku temperatuur kiiresti tõusma kuni sulamiseni. GTF võrrandit kasutav mudel jõudis sulamistemperatuurini ∼1.2 % madalama välja korral võrreldes FN mudeliga. GTF mudeli järgi leitud temperatuur oli sulamistemperatuuri lähedal ∼50 % suurem.

FEM nanoteraviku mudeli termilist ja voolude käitumist võrreldi ka hübriid elektrodünaamika - molekulaardünaamika (HELMOD) mudeliga. Fundamentaalsete pinnaesituste erinevuse tõttu oli metalli pinnal kujunev elektriväli märkimisväärselt erinev. Kogu emissioonivoolu ja tipu temperatuuri sõltuvus lokaalsest elektriväljast tipupunktis oli mõlemal mudelil sarnane, kuid esinesid ka numbrilised erinevused, mida oligi oodata.

Fowler-Nordheimi diagramm on makroskoopiliselt mõõdetud voolu ja elektrivälja andmete esitamise viis, mille joone tõusust saab hinnata pinnal olevate teravike väljavõimendustegurit β. Antud metoodika puhul eeldatakse, et emissioonivoolud alluvad Fowler-Nordheimi võrrandile. GTF mudeli puhul on aga FN diagrammil väiksemate väljade juures olulised kõrvalekalded võrreldes FN võrrandiga (eriti veel siis, kui on toimunud makroskoopiline soojenemine). Hinnatud väljavõimendustegur β_c võib kõrvalekaldunud osas meelevaldselt kasvada. Elektrivälja juures, kus teravik hakkab sulama, on samuti GTF mudeli abil leitud FN diagrammil kõrvalekalle FN mudeli omaga võrreldes. Selles osas on aga hinnatud väljavõimendustegur β_c väiksem (kuni null) kui tegelik β.

Acknowledgements

First of all, I would like to thank my supervisor Vahur Zadin, who has been my main guide in the world of science. Secondly, I thank my co-supervisor Flyura Djurabekova for helpful comments and discussions about my thesis. I am also grateful to Stefan Parviainen, who offered invaluable insight and provided the HELMOD calculations. My gratitude also goes to K. L. Jensen for interesting and clarifying discussions about the general thermal-field equation.

Additionally, I would like to thank the friendly collective at the Intelligent Materials and Systems lab and the head of the lab, Alvo Aabloo, for providing me with an excellent work and study environment. I also wish to thank the University of Tartu for providing me with the opportunity to pursue my passion of physics.

And last but not least, I express my deepest gratitude towards all family and friends who have supported me throughout my studies.

References

[1] P. Osmokrovic, M. Vujisic, J. Cvetic, and M. Pesic, "Stochastic Nature of Electrical Breakdown in Vacuum", IEEE Transactions on Dielectrics and Electrical Insulation **14**, 803–812 (2007).

[2] H. H. Braun, S. Döbert, W. Wuensch, M. Taborelli, I. V. Syratchev, and I. H. Wilson, "CLIC High-Gradient Test Results", (2002).

[3] M. Aicheler, P. Burrows, M. Draper, T. Garvey, P. Lebrun, K. Peach, N. Phinney, H. Schmickler, D. Schulte, and N. Tog, eds., *A Multi-TeV linear collider based on CLIC technology: CLIC Conceptual Design Report* (CERN, 2012).

[4] *Compact Linear Collider*, (2015) `http://clic-study.org/`.

[5] T. Higo, "Progress of X-Band Accelerating Structures", FR104 (2011).

[6] G. A. Mesyats, "Pulsed power", (2005).

[7] D. E. Post and R. Behrisch, eds., *Physics of Plasma-Wall Interactions in Controlled Fusion* (Springer US, Boston, MA, 1986).

[8] C. Antoine, F. Peauger, and F. Le Pimpec, "Erratum to: Electromigration occurences and its effects on metallic surfaces submitted to high electromagnetic field: A novel approach to breakdown in accelerators", Nuclear Instruments and Methods in Physics Research Section A: Accelerators, Spectrometers, Detectors and Associated Equipment **670**, 79–94 (2012).

[9] E. Hourdakis, G. W. Bryant, and N. M. Zimmerman, "Electrical breakdown in the microscale: Testing the standard theory", Journal of Applied Physics **100**, 123306 (2006).

[10] R. V. Latham and E. Braun, "Electron optical observations of cathode protrusions formed during pre-breakdown conditioning", en, Journal of Physics D: Applied Physics **1**, 1731–1735 (1968).

[11] A. Grudiev, S. Calatroni, and W. Wuensch, "New local field quantity describing the high gradient limit of accelerating structures", Physical Review Special Topics - Accelerators and Beams **12**, 102001 (2009).

[12] R. Marcus, K. Chin, Y. Yuan, H. Wang, and W. Carr, "Simulation and design of field emitters", English, IEEE Transactions on Electron Devices **37**, 1545–1550 (1990).

[13] S. Sun and L. K. Ang, "Analysis of nonuniform field emission from a sharp tip emitter of Lorentzian or hyperboloid shape", Journal of Applied Physics **113**, 144902 (2013).

[14]L.-J. Pegg and R. A. Hatton, "Nanoscale geometric electric field enhancement in organic photovoltaics.", ACS nano **6**, 4722–30 (2012).

[15]R. H. Fowler and L. Nordheim, "Electron Emission in Intense Electric Fields", Proceedings of the Royal Society of London. Series A **119**, 173–181 (1928).

[16]K. L. Jensen, *Electron Emission Physics*, Vol. 149, Advances in Imaging and Electron Physics (Elsevier, 2007), pp. 47–146.

[17]K. L. Jensen, "General formulation of thermal, field, and photoinduced electron emission", Journal of Applied Physics **102**, 24911 (2007).

[18]K. L. Jensen, Y. Y. Lau, D. W. Feldman, and P. G. O'Shea, "Electron emission contributions to dark current and its relation to microscopic field enhancement and heating in accelerator structures", Physical Review Special Topics-Accelerators and Beams **11**, 81001 (2008).

[19]C. Herring and M. H. Nichols, "Thermionic Emission", Reviews of Modern Physics **21**, 185–270 (1949).

[20]A. Descoeudres, Y. Levinsen, S. Calatroni, M. Taborelli, and W. Wuensch, "Investigation of the dc vacuum breakdown mechanism", Physical Review Special Topics - Accelerators and Beams **12**, 092001 (2009).

[21]a. Descoeudres, T. Ramsvik, S. Calatroni, M. Taborelli, and W. Wuensch, "Dc Breakdown Conditioning and Breakdown Rate of Metals and Metallic Alloys Under Ultrahigh Vacuum", Physical Review Special Topics - Accelerators and Beams **12**, 032001 (2009).

[22]J. Paulini, T. Klein, and G. Simon, "Thermo-field emission and the Nottingham effect", Journal of Physics D: Applied Physics **26**, 1310–1315 (1993).

[23]S. Coulombe and J.-L. Meunier, "A comparison of electron-emission equations used in arc - cathode interaction calculations", Journal of Physics D: Applied Physics **30**, 2905–2910 (1997).

[24]E. Hantzsche, "The Thermo-Field Emission of Electrons in Arc Discharges", Beiträge aus der Plasmaphysik **22**, 325–346 (1982).

[25]R. G. Forbes, "Use of energy-space diagrams in free-electron models of field electron emission", Surface and interface analysis **36**, 395–401 (2004).

[26]M. E. Kiziroglou, X. Li, A. A. Zhukov, P. A. J. De Groot, and C. H. De Groot, "Thermionic field emission at electrodeposited Ni–Si Schottky barriers", Solid-State Electronics **52**, 1032–1038 (2008).

[27]J. Orloff, *Handbook of Charged Particle Optics* (CRC Pr Llc, 2008), pp. 5–6.

[28]R. G. Forbes and J. H. Deane, "Reformulation of the standard theory of Fowler–Nordheim tunnelling and cold field electron emission", Proceedings of the Royal Society A: Mathematical, Physical and Engineering Sciences **463**, 2907–2927 (2007).

[29]R. G. Forbes, "Simple good approximations for the special elliptic functions in standard Fowler-Nordheim tunneling theory for a Schottky-Nordheim barrier", Applied physics letters **89**, 113122 (2006).

[30]E. L. Murphy and R. H. Good, "Thermionic Emission, Field Emission, and the Transition Region", Phys. Rev. **102**, 1464–1473 (1956).

[31]R. G. Forbes, C. Edgcombe, and U. Valdrè, "Some comments on models for field enhancement", Ultramicroscopy **95**, 57–65 (2003).

[32]S. Parviainen, F. Djurabekova, H. Timko, and K. Nordlund, "Electronic processes in molecular dynamics simulations of nanoscale metal tips under electric fields", Computational Materials Science **50**, 2075–2079 (2011).

[33]J. P. Barbour, W. W. Dolan, J. K. Trolan, E. E. Martin, and W. P. Dyke, "Space-Charge Effects in Field Emission", Physical Review **92**, 45–51 (1953).

[34]V. G. Pavlov, "Effect of the space charge of emitted electrons on field electron emission", Technical Physics **49**, 1610–1616 (2004).

[35]F. Djurabekova, S. Parviainen, A. Pohjonen, and K. Nordlund, "Atomistic modeling of metal surfaces under electric fields: Direct coupling of electric fields to a molecular dynamics algorithm", Physical Review E **83**, 026704 (2011).

[36]R. A. Matula, "Electrical resistivity of copper, gold, palladium, and silver", Journal of Physical and Chemical Reference Data **8**, 1147 (1979).

[37]C. E. Schuster, M. G. Vangel, and H. Schafft, "Improved estimation of the resistivity of pure copper and electrical determination of thin copper film dimensions", Microelectronics Reliability **41**, 239–252 (2001).

[38]Y. S. Touloukian, R. K. Kirby, R. E. Taylor, and P. D. Desai, "Thermophysical Properties of Matter - the TPRC Data Series. Volume 12. Thermal Expansion Metallic Elements and Alloys", (1975).

[39]B. Feng, Z. Li, and X. Zhang, *Role of phonon in the thermal and electrical transports in metallic nanofilms*, May 2009.

[40]R. J. Elliott and A. F. Gibson, *An Introduction to Solid State Physics and Its Applications* (Macmillan, 1974), p. 490.

[41]P. Nath and K. Chopra, "Thermal conductivity of copper films", Thin Solid Films **20**, 53–62 (1974).

[42]Z. Zhang, *Nano/Microscale Heat Transfer* (McGraw Hill Professional, 2007), p. 479.

[43]R. B. Dingle, "The Electrical Conductivity of Thin Wires", Proceedings of the Royal Society A: Mathematical, Physical and Engineering Sciences **201**, 545–560 (1950).

[44]A. Yarimbiyik, H. Schafft, R. a. Allen, M. Zaghloul, and D. L. Blackburn, "Modeling and simulation of resistivity of nanometer scale copper", Microelectronics Reliability **46**, 1050–1057 (2006).

[45]A. Yarimbiyik, M. Zaghloul, and H. Schafft, *Implementation of simulation program for modeling the effective resistivity of nanometer scale film and line interconnects*, 2006.

[46]A. Yarimbiyik, H. A. Schafft, R. A. Allen, M. D. Vaudin, and M. E. Zaghloul, "Experimental and simulation studies of resistivity in nanoscale copper films", Microelectronics Reliability **49**, 127–134 (2009).

[47]E. H. Sondheimer, "The mean free path of electrons in metals", Advances in Physics **50**, 499–537 (2001).

[48]H. H. Mende and G. Thummes, "Surface scattering of electrons on copper whiskers and its influence on the electrical resistivity at 4.2 K", Applied Physics **6**, 93–97 (1975).

[49]D. Jou, V. Cimmelli, and A. Sellitto, "Nonlocal heat transport with phonons and electrons: Application to metallic nanowires", International Journal of Heat and Mass Transfer **55**, 2338–2344 (2012).

[50]W. Zhu, *Vacuum microelectronics* (Wiley, 2001).

[51]O. C. Zienkiewicz, R. L. Taylor, and J. Zhu, *The Finite Element Method: Its Basis and Fundamentals* (Butterworth-Heinemann, 2005), p. 752.

[52]C. Grossmann and H.-G. Roos, *Numerical Treatment of Partial Differential Equations* (Springer Science and Business Media, 2007), p. 591.

[53]G. Liu and S. S. Quek, *The Finite Element Method: A Practical Course* (Elsevier Science, 2013), p. 464.

[54]P.-b. Zhou, *Numerical Analysis of Electromagnetic Fields* (Springer Berlin Heidelberg, 2012), p. 406.

[55]S. S. RAO, *The Finite Element Method in Engineering* (Butterworth-Heinemann, 2011), p. 688.

[56]*COMSOL Multiphysics 5.0 User's Guide*, 2014.

[57]*PARDISO 5.0.0 Solver Project*, 2015.

[58]A. Kuzmin, M. Luisier, and O. Schenk, "Fast Methods for Computing Selected Elements of the Greens Function in Massively Parallel Nanoelectronic Device Simulations", in *Euro-par 2013 parallel processing*, Vol. 8097, edited by F.˜Wolf, B.˜Mohr, and D.˜Mey, Lecture Notes in Computer Science (Springer Berlin Heidelberg, 2013), pp. 533–544.

[59]O. Schenk, M. Bollhöfer, and R. A. Römer, "On Large-Scale Diagonalization Techniques for the Anderson Model of Localization", SIAM Rev. **50**, 91–112 (2008).

[60]O. Schenk, A. Wächter, and M. Hagemann, "Matching-based preprocessing algorithms to the solution of saddle-point problems in large-scale nonconvex interior-point optimization", Computational Optimization and Applications **36**, 321–341 (2007).

[61]*MUMPS: a MUltifrontal Massively Parallel sparse direct Solver*, 2015.

[62]*Multiphysics Modeling and Simulation Software - COMSOL*, 2013.

[63]S. Lagotzky, P. Serbun, G. Müller, S. Calatroni, and T. Muranaka, "ENHANCED FIELD EMISSION AND EMITTER ACTIVATION ON FLAT DRY-ICE CLEANED CU SAMPLES", in 5th international particle accelerator conference ipac'14 (June 2014).

[64]F. Charbonnier, R. Strayer, L. Swanson, and E. Martin, "Nottingham Effect in Field and T-F Emission: Heating and Cooling Domains, and Inversion Temperature", Physical Review Letters **13**, 397–401 (1964).

[65]I. A. Blech and C. Herring, "Stress generation by electromigration", Applied Physics Letters **29**, 131 (1976).

Non-exclusive licence to reproduce thesis and make thesis public

I, Kristjan Eimre

1. herewith grant the University of Tartu a free permit (non-exclusive licence) to:
   (a) reproduce, for the purpose of preservation and making available to the public, including for addition to the DSpace digital archives until expiry of the term of validity of the copyright, and
   (b) make available to the public via the web environment of the University of Tartu, including via the DSpace digital archives, as of 26.05.2020 until expiry of the term of validity of the copyright,

   Implementing the general thermal-field emission equation to the high electric field nanoprotrusion model,

   supervised by Vahur Zadin and Flyura Djurabekova,
2. I am aware of the fact that the author retains these rights.
3. I certify that granting the non-exclusive licence does not infringe the intellectual property rights or rights arising from the Personal Data Protection Act.

Tartu, May 29, 2015